Published in final edited form as:
Mol Cell. 2024 January 18; 84(2): 293–308.e14. doi:10.1016/j.molcel.2023.11.027.

Multisite phosphorylation dictates selective E2-E3 pairing as revealed by Ubc8/UBE2H-GID/CTLH assemblies

Jakub Chrustowicz[1,5], **Dawafuti Sherpa**[1,5], **Jerry Li**[2], **Christine R. Langlois**[1], **Eleftheria C. Papadopoulou**[1,4], **D. Tung Vu**[3], **Laura A. Hehl**[1,4], **Özge Karayel**[3], **Viola Beier**[1], **Susanne von Gronau**[1], **Judith Müller**[1], **J. Rajan Prabu**[1], **Matthias Mann**[3], **Gary Kleiger**[2], **Arno F. Alpi**[1], **Brenda A. Schulman**[1,4,6,*]

[1]Department of Molecular Machines and Signaling, Max Planck Institute of Biochemistry, Martinsried 82152, Germany

[2]Department of Chemistry and Biochemistry, University of Nevada, Las Vegas, NV 89154, USA

[3]Department of Proteomics and Signal Transduction, Max Planck Institute of Biochemistry, Martinsried 82152, Germany

[4]Technical University of Munich, School of Natural Sciences, Munich 85748, Germany

[5]These authors contributed equally

[6]Lead contact

SUMMARY

Ubiquitylation is catalyzed by coordinated actions of E3 and E2 enzymes. Molecular principles governing many important E3-E2 partnerships remain unknown, including for RING-family GID/CTLH E3 ubiquitin ligases and their dedicated E2, Ubc8/UBE2H (yeast/human nomenclature). GID/CTLH-Ubc8/UBE2H-mediated ubiquitylation regulates biological processes ranging from yeast metabolic signaling to human development. Here, cryo-EM, biochemistry, and cell biology reveal this exquisitely specific E3-E2 pairing through an unconventional catalytic assembly and auxiliary interactions 70–100 Å away, mediated by E2 multisite phosphorylation. Rather than dynamic polyelectrostatic interactions reported for other ubiquitylation complexes, multiple Ubc8/UBE2H phosphorylation sites within acidic CK2-targeted sequences specifically anchor the E2 C-termini to E3 basic patches. Positions of phospho-dependent interactions relative to the catalytic domains correlate across evolution. Overall, our data show that phosphorylation-dependent

---

*Correspondence: schulman@biochem.mpg.de.

AUTHOR CONTRIBUTIONS
Conceptualization: J.C., D.S., B.A.S.; Biochemistry: J.C., D.S., E.C.P.; Cryo-EM, structure building, and refinement: J.C., D.S., J.R.P; Enzyme kinetics: J.L., G.K.; Cell biology: J.M., A.F.A.; Protein purification: J.C., D.S., E.C.P.; Protein expression: J.C., D.S., E.C.P., S.vG.; Yeast substrate degradation assays: D.S., C.R.L., L.A.H., V.B.; Proteomics: D.T.V., Ö.K., M.M.; Data analysis and writing of the manuscript: J.C., D.S., B.A.S, Funding: M.M, G.K., B.A.S.

DECLARATION OF INTERESTS
B.A.S. is adjunct faculty at St. Jude Children's Research Hospital, member of the scientific advisory boards of BioTheryX and Proxygen, and co-inventor of intellectual property licensed to Cinsano.

multivalency establishes a specific E3-E2 partnership, is antagonistic with dephosphorylation, rigidifies the catalytic centers within a flexing GID E3-substrate assembly, and facilitates substrate collision with ubiquitylation active sites.

eTOC Blurb

Chrustowicz, Sherpa, et al. decipher evolutionarily conserved determinants of an exquisitely specific E3-E2 partnership ubiquitylating globular substrates. Cryo-EM visualizes a flexing GID E3 superassembly channeling its substrate between two ubiquitylation active sites. The catalytic architecture depends on multivalent Ubc8/UBE2H-GID/CTLH E3 contacts between multiphosphorylated E2 extensions and complementary E3 basic patches.

Graphical abstract

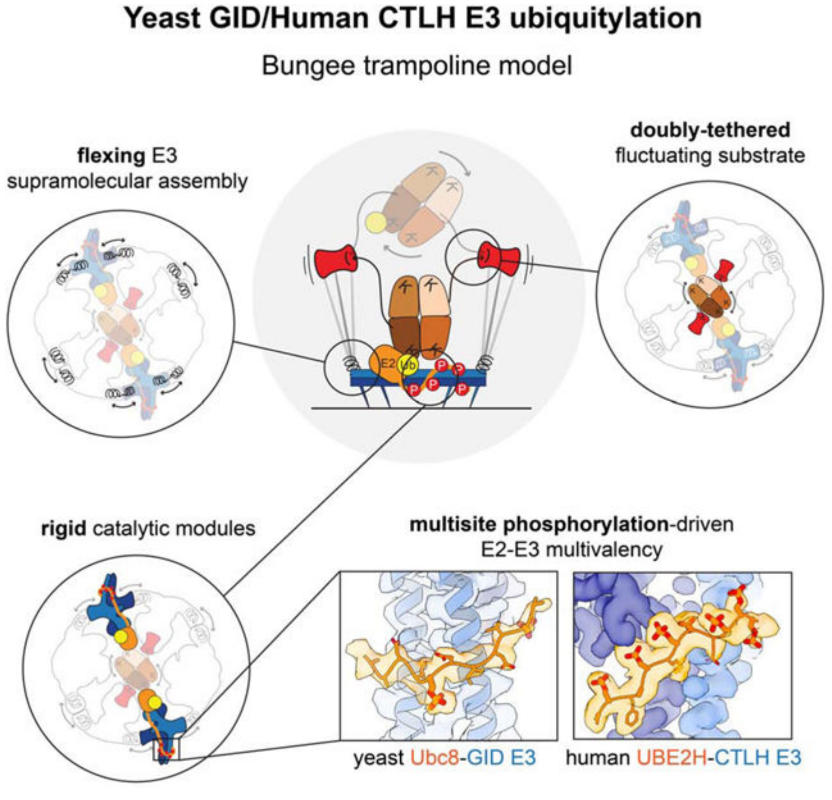

INTRODUCTION

Ubiquitylation is a major eukaryotic post-translational modification that orchestrates myriad signaling pathways and maintains homeostasis. Specific proteins become ubiquitylated by tri-enzyme E1-E2-E3 cascades catalyzing the modification[1–3]. After E1-catalyzed linkage of ubiquitin’s C-terminus to an E2’s catalytic cysteine, the resultant E2~ubiquitin conjugate collaborates with a partner E3 (‘~’ here denotes covalent linkage of ubiquitin to E2 active site). E3s recruit substrates for ubiquitylation by recognizing specific motifs, termed ‘degrons’. In humans, innumerable such pathways are established by two ubiquitinactivating (E1), ≈40 ubiquitin-conjugating (E2) and ≈600 ubiquitin ligase (E3) enzymes. Thus, it is of great interest to understand how E2~ubiquitin-E3 complexes are configured to achieve modification. To date, structural studies have largely focused on how E2s with broad sets of E3 partners modify peptide-like substrates[4,5]. However, some E2s are dedicated to particular E3s and vice-versa, and cellular ubiquitylation occurs on substrates with diverse structural features. Nonetheless, molecular understanding of why specific E2s are employed by certain E3s remains rudimentary. Moreover, there is little structural data suggesting how E2-E3 complexes ubiquitylate globular substrates on multiple sites.

One dedicated E2-E3 combination of emerging interest is the Ubc8-GID complex in budding yeast, and its counterpart, the UBE2H-CTLH complex, in higher organisms. This E2-E3 partnership was discovered through identification of budding yeast mutants deficient in glucose-induced degradation of the gluconeogenic enzyme fructose-1,6-bisphosphatase (Fbp1) under metabolic conditions when Fbp1 activity is superfluous and energetically unfavorable to maintain[6–8]. The identified genes encode proteins named Gid#. Gid3 corresponds to the E2, Ubc8[8], and the majority of other Gid proteins are subunits of a multiprotein ‘GID’ E3 that regulates ubiquitylation-mediated degradation of enzymes involved in gluconeogenesis and other metabolic pathways[9–12]. The corresponding *Drosophila* UBE2H-CTLH E3 pathway plays critical roles in embryogenesis[13,14]. Furthermore, UBE2H and CTLH subunits in mammals and other higher eukaryotes have been associated with roles in signaling and metabolism[15–23], are transcriptionally co-upregulated in erythroid progenitors[24–26], contribute to orderly erythropoiesis[27–29], and are essential for proper development[30–32]. Given the important physiological roles of UBE2H-CTLH complexes and their potential suitability for mediating targeted protein degradation[33–35], it is important to understand the molecular underpinnings of this highly specific E2-E3 pairing.

Prior structural studies revealed an assortment of GID/CTLH E3 assemblies, which vary by incorporation of different interchangeable substrate-binding subunits, and by higher-order association of an evolutionarily conserved core catalytic assembly[11,17,36–39]. The biochemical mechanisms are best understood for budding yeast Ubc8-GID complexes, for which substrate ubiquitylation has been reconstituted *in vitro* and glucose-induced degradation has been interrogated *in vivo* for genetically-validated substrates[36,37]. These studies revealed a core assembly, termed GID^{SR4}, composed of two modules. A substrate receptor scaffolding module (Gid1-Gid8-Gid5 subcomplex) binds the glucose-induced substrate-binding subunit Gid4 (‘SR4’ in GID^{SR4} refers to the substrate receptor subunit number), which in turn binds substrate Pro/N-degrons (degrons featuring an N-terminal proline)[6,36,40–43]. A catalytic module (Gid2-Gid9 subcomplex) features a RING domain from Gid2 and RING-Like (RINGL) domain from Gid9, and catalyzes ubiquitylation with the Ubc8~ubiquitin conjugate[37]. GID^{SR4} is sufficient to regulate some gluconeogenic substrates[36]. However, Fbp1 degradation is controlled by a different assembly called ‘Chelator-GID^{SR4}’, wherein two GID^{SR4} subcomplexes and additional subunits form a hollow oval structure[37,44]. Chelator-GID^{SR4} simultaneously captures flexibly-tethered Pro/N-degrons from two of four Fbp1 protomers. The tetrameric globular domain of Fbp1 containing the ubiquitylation sites is encapsulated in the center of the oval-shaped E3 complex. Despite this progress, the catalytic assembly formed by a GID/CTLH E3 and its dedicated ubiquitin-conjugated E2, Ubc8/UBE2H, remains elusive.

Here, structures of GID/CTLH E3 complexes with stable mimics of Ubc8/UBE2H~ubiquitin conjugates reveal elaborate multimodal E2-E3-substrate interactions. Unexpectedly, extensions C-terminal of the catalytic ‘UBC’ domains of yeast Ubc8 and human UBE2H harbor multiple phosphorylation sites that engage basic patches on their partner E3 catalytic module and potentiate ubiquitylation. The precise nature of these interactions differs from previously-characterized electrostatically-driven E3 complexes that are thought to be conformationally heterogeneous[45–48]. The structural data suggest that phosphorylation-dependent anchoring of the catalytic module in the context of a flexing Chelator-GID^{SR4} complex facilitates channeling of the Fbp1 substrate to the ubiquitylation active sites. Overall, our data illuminate the Ubc8/GID-family E2-E3 ubiquitylation machinery, and a conserved structural role for E2 multisite phosphorylation.

RESULTS

Cryo-EM shows substrate channeling between GID E3 active sites

To gain structural insights into how the substrate Fbp1 approaches ubiquitylation active sites, we obtained cryo-EM data for a complex composed of Chelator-GID^{SR4}, Fbp1, and a stable proxy for the Ubc8~ubiquitin intermediate with ubiquitin’s C-terminus isopeptide-bonded to a lysine replacement for Ubc8’s catalytic cysteine. The Chelator-GID^{SR4} and Ubc8 were prepared from a eukaryotic source, by baculoviral expression in insect cells, while Fbp1 and ubiquitin were prepared using standard protocols for expression in *E. coli*. The cryo-EM data refined to five classes that visualized all components at ≈16–20 Å resolution (Figure S1A). As expected based on prior structures[36,37], fitting the maps with published coordinates and structural models showed the Fbp1 substrate encapsulated at the center of the oval-shaped E3-E2~ubiquitin assembly (Figure S2A). The two copies of the catalytic module, each comprising the RING and RINGL subunits Gid2 and Gid9 and one asymmetrically positioned Ubc8~ubiquitin conjugate, are located on opposite sides of the oval. Their active sites face the central Fbp1 substrate.

Visualizing the different classes as frames in a movie revealed three unexpected features suggesting that multiple Fbp1 protomers are channeled between ubiquitylation active sites (Video S1). First, the flexibly tethered substrate, Fbp1, samples multiple positions relative to the catalytic centers. While one pair of the substrate’s target lysines approaches an active site in three of five classes, scanning between the structures shows that Fbp1 essentially bounces around inside the enclosure of the ubiquitylation complex (Figures 1A and S2A). Second, Chelator-GID^{SR4} is itself pliable, with its shape varying between more oval and more circular silhouettes. We surmise that the Chelator-GID^{SR4} axes expand and contract through twisting and turning of spring-like helical CTLH-CRA^{N} domains at the intermodular junctions[37], enabling dynamic reshaping of the entire complex during catalysis (Figure 1B). Finally, despite the dynamic nature of the GID E3-Ubc8~ubiquitin-substrate assembly, the catalytic module itself is a remarkably rigid 140 Å-long tower-like unit, with securely affixed RING domains and the Ubc8~ubiquitin conjugate at one end. It seems this constrained configuration limits degrees of freedom of the catalytic complex, thus facilitating collision with the fluctuating substrate (Figure S2B).

Multimodal interactions specify Ubc8~ubiquitin-GID pairing

The relatively fixed arrangement of the catalytic module was perplexing, as this differs from the dynamic catalytic modules formed by other multiprotein E3s such as cullin-RING ligases or APC/C[49–51]. Key elements determining the unique E2-E3 coupling emerged from a ≈5-Å resolution focused-refined map, which accommodated previously determined coordinates for the GID E3 subcomplex, Ubc8 and ubiquitin (Figure 1C). Unexpectedly, additional tubular density projects from the C-terminus of Ubc8's catalytic UBC domain, extending 40 Å to contact the junction between Gid9's CTLH-CRA^{N} and coiled-coil domains. Then, it traverses another 80 Å, across the Gid2 portion of the coiled-coil, around the distal edge, and ultimately lodging at the surface of the coiled-coil adjacent to the Gid2-Gid9 interface. We attribute this additional density to Ubc8's C-terminal extension.

An atomic model built from a 3.5-Å resolution focused-refined map revealed molecular underpinnings of the tower-shaped catalytic assembly between Gid2-Gid9 and Ubc8~ubiquitin (Figures 2, S1B and S1C, Table S1). The GID E3 catalytic domain centers around the Gid2 RING, but contains many unique features that specifically conform to Ubc8 and extend interactions far beyond those typical for RING-type E3s with conserved E2 UBC domains[52–55]. While the Gid2 RING adopts a canonical fold, it resembles the catalytic Siz/PIAS RING (SP-RING) domains of SUMO E3s in coordinating only one zinc structuring the Ubc8~ubiquitin-interacting loops[56,57] (Figure S2C). Moreover, one face of the Gid2 RING forms the side of a deep bowl-shaped surface (Figure 2A). The bowl's base is the end of the Gid9 'belt', which encases the Gid2 and Gid9 RING and RINGL domains. The other side is formed by Gid2's CRA^{C} helix and ensuing loop. Together, these elements surround Ubc8's N-terminal surface, including the entire solvent-exposed portion of Helix-1 and the following strand and loop, which do not typically participate in RING E3-E2 interactions. Notably, substituting Gid2's V334 with residues designed to repel interactions with Ubc8 Helix-1 diminished substrate ubiquitylation, whereas extending the hydrophobic interface by swapping A332 with a tryptophan had a slightly stimulating effect (Figure 2C).

The opposite face of Gid2's RING binds Gid9's unique RINGL domain in the assembly stabilizing the Ubc8~ubiquitin conjugate in a 'closed' conformation (Figures 2A and S2D). In the closed conformation, interactions between an E2 and its linked ubiquitin strain the active site for nucleophilic attack by a substrate lysine[52,54,55]. The Ubc8~ubiquitin conformation is stabilized by some canonical dimeric RING E3 features – hydrophobic RING-E2 interactions between Gid2 (V363, L364, L391) and Ubc8 'L1' (P60, Y61) and 'L2' (P95) elements, and a 'non-RING priming' ubiquitin-binding element (Y514) from Gid9 (Figure 2A). However, Gid2's RING lacks a canonical 'linchpin' arginine[55,58,59]. Instead, its first loop displays K365 as an alternative linchpin inserting between Ubc8 and its conjugated ubiquitin on the side opposite from the active site. Mutation of these elements nearly abolished GID^{SR4} and Ubc8-mediated ubiquitylation of a peptide substrate, corroborating their previously reported requirements for glucose-induced degradation of Fbp1[36] (Figures 2B and 2C). Also, the loops from Gid2's RING domain serve as glues between Ubc8 and ubiquitin. Notably, mutation of Y403, which projects from the zinc-binding loop of Gid2 and inserts into the opening of ubiquitin's hydrophobic core, attenuated ubiquitylation (Figures 2A and 2C). Interestingly, the angle between Ubc8 and ubiquitin is larger than that in other RING E3E2~ubiquitin complexes[52–55,60] due to protrusion of Ubc8's W105 into ubiquitin's L8/V70/L71 hydrophobic pocket (Figure S2E). This conformation resembles catalytic complexes between ubiquitin-like proteins NEDD8 and SUMO and their cognate E2s[56,58].

At the opposite end of the complex, Ubc8's C-terminal extension docks with an 80-Å long basic patch spanning much of the Gid2-Gid9 coiled-coil (Figure 2D). Although the upstream part of Ubc8's C-terminal extension is blurred in the higher-resolution reconstruction, 11 residues proximal to the C-terminus were modeled engaging the Gid2 edge of the E3 coiled-coil (Figure 2E). This sequence was distinguished by hydrophobic residues punctuating a stretch of serines and acidic residues. Strikingly, bulky density surrounding hydroxyls from two serines supported fitting phosphoserines. Phosphorylation could have arisen during Ubc8 expression in insect cells. Thus, the structure suggested phosphorylation-mediated Ubc8-GID interactions could synergize with the distinctive catalytic assembly in this dedicated E2-E3 pair.

C-terminal extensions of Ubc8 and UBE2H are phosphorylated at multiple sites

Intrigued by our structural findings, we inspected the sequence of the Ubc8 C-terminal extension, which led to three conclusions (Figure 3A). First, it is highly acidic, consistent with complementing a basic patch on the GID E3. Second, the acidic stretch is punctuated by a few hydrophobic residues. Third, it is remarkably rich in serine, and to a lesser extent threonine residues, raising the possibility of additional phosphorylation sites beyond those visible in the structure (Figure 2E). Indeed, multiple species were observed for insect cell-expressed (IC) Ubc8 upon comparing its intact mass with that treated with lambda phosphatase (λPP), or Ubc8 expressed in bacterial cells (BC) (Figure 3B). The molecular weights were consistent with IC Ubc8 modification with up to 9 phosphates. Furthermore, the human UBE2H C-terminal extension, whilst 37 residues shorter than its yeast ortholog, likewise contains numerous serines and acidic residues, with interspersed hydrophobic amino acids (Figure 3A). Intact mass analysis revealed that IC UBE2H is indeed multi-phosphorylated (Figure 3B). Thus, we hypothesized that phosphorylation-mediated E2-E3 interactions would be evolutionarily conserved.

We sought to map the region of Ubc8/UBE2H multisite phosphorylation. Unfortunately, we were unable to devise a proteomics method identifying phosphorylation sites within the E2 C-terminal extensions due to challenges imposed by the highly acidic peptides formed upon their enzymatic fragmentation. Thus, we examined effects of mutations using Phos-tag technology, which reduces migration of phosphorylated proteins in SDS-PAGE. In agreement with the intact mass spectrometry data, the IC E2s migrated as multiple bands, slower than their unphosphorylated counterparts (λPP-treated and BC) (Figure 3C). Mutation of C-terminal serine and threonine residues, or progressive C-terminal deletions, shifted the banding pattern proportionately with the number of remaining potential phosphosites, suggesting all of them might be phosphorylated. Similar to the purified proteins, mutating the C-terminal extension of 3xFLAG-tagged UBE2H transiently expressed in HEK293 cells abolished its phosphorylation (Figure 3D). Thus, Ubc8 and UBE2H C-terminal extensions are multi-phosphorylated in eukaryotic cells.

E2 phosphorylation potentiates interactions with E3, and E3-dependent ubiquitylation

Several initial experiments indicated functional importance of Ubc8/UBE2H phosphorylation. First, phosphorylation potentiates E2-E3 interactions. IC E2s, but not unphosphorylated versions, co-purified their cognate recombinant GID/CTLH E3 complexes from insect cell lysates (Figure 3E), and bacterially-expressed catalytic subunits (Figure S3A). Accordingly, as measured by BioLayer Interferometry (BLI), the phosphorylated IC UBE2H binds the CTLH subcomplex with submicromolar affinity (0.8 μM K_D). This is far superior to that of BC UBE2H, which showed marginal binding even at the highest E3 concentration tested (Figures 3F and S4A). Moreover, the CTLH complex selectively co-immunoprecipitated with wild-type (WT) 3xFLAG-UBE2H expressed in HEK293 cells (Figure 3G, Table S2). This was impaired by mutation of UBE2H C-terminal serines, pointing towards phosphorylation-dependence of this exquisite E2-E3 pairing. Second, E2 phosphorylation substantially increases ubiquitylation of model peptide substrates (with a Gid4-binding N-degron and optimally-spaced target lysine, Figure 3H), and of Mdh2 and Fbp1 (Figure S3B) by their cognate GID/CTLH E3 complexes. Comparing reactions with WT ubiquitin and that devoid of lysines (K0 Ub) showed that IC Ubc8 synthesized chains with more ubiquitins, and modified more sites on these substrates, during their single encounter with the catalytic assembly (Figures S3C and S3D). Finally, querying lysine-induced discharge of ubiquitin from its conjugated E2 showed phosphorylation only boosts E3-dependent activity (Figures S3E and S3F).

To gain mechanistic insights, we performed kinetic analyses of GID-mediated substrate ubiquitylation by titrating various versions of Ubc8. Strikingly, compared with the BC version, IC Ubc8 displayed a seven-fold lower K_m of 500 nM, consistent with Ubc8 phosphorylation enhancing binding to the GID E3 (Figures 3I and S4B). Moreover, phosphorylation exerted an even more dramatic effect on catalysis: the IC Ubc8 displayed 20-fold higher observed reaction turnover number k_{obs} than the BC version (Figures 3I and S4C). This could be rationalized if interactions mediated by Ubc8's phosphorylated C-terminal extension enhance productive E3 encounter by the ubiquitin-conjugated UBC domain. Overall, Ubc8 phosphorylation improves catalytic efficiency (k_{obs}/K_m) of substrate ubiquitylation by a striking 140-fold (Figure 3I). Accordingly, mutation of the Ubc8 phosphorylation sites *in vivo* abrogated glucose-induced degradation of gluconeogenic substrates targeted by various GID E3 assemblies (Figures 3J and S3G).

Consistent with a role for increased negative charge density brought about by multisite phosphorylation, replacing all Ubc8 C-terminal serines and threonines with aspartates improved catalytic efficiency 30-fold relative to the WT BC version (Figures 3I, S4B and S4C). Nonetheless, this mutant was nearly 5-fold less efficient *in vitro* than IC Ubc8 and did not promote glucose-induced degradation of yeast Fbp1 *in vivo* (Figure 3J). Although the phosphomimetic UBE2H variant bound the CTLH E3 better than its wild-type BC version as measured by BLI, its affinity was still inferior to that of IC UBE2H (Figures 3F and S4A). Thus, optimal Ubc8/UBE2H interactions with the GID/CTLH E3 seem to require molecular features of their phosphorylated C-terminal extensions.

Multiple Ubc8/UBE2H C-terminal phosphorylation sites are required to potentiate GID/CTLH E3 function

We sought to determine relative contributions of the numerous phosphorylation sites. For both yeast and human, significant impairment of GID/CTLH E3-mediated substrate ubiquitylation required mutating all the E2 phosphosites (Figures 4A–4C, 4G, S4B and S4C). Marginal defects were observed upon substituting subsets of serines and threonines in clusters. However, partial deletions of the E2 C-terminal extensions were more detrimental, albeit to different extents between organisms. For Ubc8, removal of the last 30% of its C-terminal extension – including the phosphorylation sites visible at high resolution by cryo-EM – severely abolished activity *in vitro* (Figures 4A and 4B). Since alanine replacement of phosphoserines located in this region impaired glucose-mediated degradation of Fbp1 *in vivo* (Figure 4D), it seems that this distal Ubc8 portion might be crucial for anchoring the more transiently bound upstream part to the E3. In support of this, mutating the corresponding portion of the Gid2 basic patch impeded GID activity *in vitro* and *in vivo* (Figures 4E and 4F). By contrast, successive truncations of the much shorter UBE2H C-terminal extension had progressively greater deleterious effects on substrate ubiquitylation (Figure 4G). Moreover, in HEK293 cells, the ability of transiently-expressed 3xFLAG-tagged UBE2H to co-precipitate endogenous CTLH E3 subunits was critically dependent on the presence of all phosphosite clusters, suggesting their synergistic roles (Figure 4H).

C-terminal extensions of Ubc8 and UBE2H can be phosphorylated by CK2

Considering the crucial role of Ubc8/UBE2H phosphorylation, we sought potential kinases capable of this modification. Thus, we submitted the sequences of Ubc8 and UBE2H C-terminal extensions to the kinase prediction tool NetPhos v3.1[61], which revealed three major acidophilic kinases – casein kinase 1 (CK1), casein kinase 2 (CK2) and glycogen synthase kinase 3 (GSK3) as top candidates (Figures 5A, S5A and S5B). Notably, CK2 was the major hit for most of the possible phosphorylation sites. To interrogate their potential roles, we devised an assay monitoring phosphorylation status of fluorescently-labeled BC Ubc8 and UBE2H upon incubation with yeast or HEK293 lysates as sources of kinases. Migration on Phos-tag gels showed phosphorylation by an endogenous kinase in a C-terminal extension-dependent manner (Figure 5B and S5C). Testing effects of specific chemical inhibitors of CK1, CK2 and GSK3 separately and in combination showed markedly impaired phosphorylation only by the CK2 inhibitor.

We verified CK2 can phosphorylate C-terminal extensions of Ubc8 and UBE2H with purified components (Figure 5C). Intact mass analyses indicated recombinant CK2 targets all C-terminal serine and threonine residues of both E2s (Figure 5D). Also, complete CK2-dependent phosphorylation of BC Ubc8 and UBE2H boosted activity to a level similar to the IC E2s (Figures S4B, S4C, S5D and S5E).

Since *in vivo* degradation of a GID substrate requires phosphosites from Ubc8's C-terminal extension (Figure 3J), we tested if this is also affected by CK2. In yeast, two redundant isoforms of the CK2 catalytic subunit, CK2α and CK2α', are encoded by *CKA1* and *CKA2* genes, respectively. Although CK2 is an essential kinase, and co-deletion of both α-subunit isoforms is lethal[62], deletion of either *CKA1* or *CKA2* delayed glucose-induced degradation of Fbp1 (Figure 5E).

Structural basis for multisite phosphorylation-dependent UBE2H binding to CTLH E3

The structural and mutational data indicated that the distal-most region of Ubc8's phosphorylated C-terminal extension plays a crucial role, serving as a GID E3 anchor 80 Å away from its catalytic ubiquitin-loaded UBC domain. However, the C-terminal extension of human UBE2H is 37 residues shorter, and its crucial region could not extend such a distance from the UBC domain. Thus, to understand how human UBE2H's phosphosites interact with the CTLH E3, we obtained a 3.4-Å resolution focused-refined cryo-EM map of a stable mimic of the phosphorylated UBE2H~ubiquitin conjugate bound to the catalytic module (the human RMND5A-MAEA subcomplex, corresponding to yeast Gid2-Gid9) (Figures 6A, S6A and S6B; Table S1). As expected, the resultant structure showed bipartite interactions between E2~ubiquitin and E3 (Figures 6A and S7A). At one end, the E3's heterodimeric catalytic domain – with RING and U-box domains from RMND5A and MAEA, respectively (Figures S7B and S7C), and RMND5A CRA^{C} and MAEA belt elements – cradles the UBE2H UBC domain and secures its conjugated ubiquitin in the closed conformation (Figure S7D). Accordingly, structure-based point mutations of RMND5A and MAEA residues stabilizing the closed UBE2H~ubiquitin conformation, and those embracing the N-terminal surface of UBE2H's UBC domain, affected ubiquitylation similarly to their counterparts in yeast GID (Figures S7E and S7F).

Much of the UBE2H C-terminal extension, including all seven phosphoserines, engages a basic patch on the CTLH E3 (Figures 6A and 6B). The phosphorylated UBE2H C-terminal residues are located only 35 Å from the UBC domain. They traverse the 30 Å long by 15 Å wide E3 basic patch, starting from the junction between RMND5A and MAEA coiled-coil helices, and extending to the MAEA groove between its coiled-coil and CTLH-CRA^{N} domain (Figure 6C).

The precise placement of seven proximate phosphorylated residues differs from other complexes where multisite phosphorylation drives dynamic sampling of varying arrangements via electrostatic interactions[47,48]. The phosphorylation-mediated interactions are established by UBE2H's C-terminal extension adopting an extended structure. This initiates from phosphoserines at residues 164, 165, 166 and E167, visible at low contour, protruding from UBE2H and contacting R88 and K91 from RMND5A (Figures 6B and 6C). Subsequent phosphoserines 168, 169, 171, and 174, clearly visible at high resolution, project from one side of the UBE2H C-terminal extension and interact with RMND5A H83 and MAEA R34, K38, H183, K186, R188, R190 and K191. Mutation of these basic MAEA and RMND5A residues inhibited ubiquitylation mediated by IC UBE2H to a similar extent as deleting the phosphorylated part of its C-terminal extension or performing the reaction with BC UBE2H (Figure 6D). The importance of the basic patch *in vivo* was shown by reduction of endogenous UBE2H co-purifying with CTLH E3 from HEK293 cells upon mutating its MAEA component (Figure S7G). In addition to the extensive electrostatic interactions, hydrophobic sidechains from UBE2H M170 and F173 insert into aliphatic pockets on the

E3 (Figures 6B, 6C and S7H). These UBE2H residues are also important for ubiquitylation (Figure 4G).

UBE2H-CTLH interactions are antagonistic with dephosphorylation and vice-versa

Phosphorylation is a reversible modification. We queried the impact of dephosphorylation on UBE2H-CTLH interactions, and vice-versa, using the nonspecific phosphatase λPP. First, we examined association of fluorescently-labeled UBE2H with CTLH E3 complexes based on migration in native PAGE. Phosphorylated UBE2H and the stable mimic of the UBE2H~ubiquitin conjugate co-migrated with the CTLH E3 in a basic patch-dependent manner (Figure 6E). Dephosphorylation of UBE2H by treatment with λPP prior to adding the E3 abrogated binding (Figures 6E and S7I). λPP treatment also substantially reduced UBE2H~ubiquitin binding to the CTLH complex. Here, ubiquitin-linked to the E2 UBC domain would increase interactions with the catalytic domain, and presumably enabling limited interactions between the dephosphorylated yet still highly acidic UBE2H C-terminus and the E3.

Next, we tested if E2-E3 interactions restrict phosphatase access. Indeed, as detected by Phos-tag gel, dephosphorylation of UBE2H and UBE2H~ubiquitin by λPP was, respectively, partially or fully blocked by pre-incubation with a WT CTLH complex but not its basic patch mutant (Figure 6F). The data indicate that binding of the phosphorylated UBE2H C-terminal extension to the E3 basic patch protects it from dephosphorylation, which is re-enforced by multimodal contacts within the complete UBE2H~ubiquitin-CTLH catalytic assembly.

Correlation between length of Ubc8/UBE2H C-terminal extension and GID/CTLH E3 basic patch across evolution

The E3 location visibly engaged by the C-terminal most phosphoserines differed strikingly for the yeast and human E2s. The former is distal while the latter is proximal to the catalytic domain that activates ubiquitin transfer from the E2. To gain insight into evolution of the basic patch, we examined its locations in AlphaFold2-generated models of catalytic modules from several evolutionarily distant organisms (Figure 7A). While the distal basic patch in the coiled-coil region is found only in some yeast, for example *S. cerevisiae* and *K. marxianus*, the basic patch that is proximal to the Gid9/MAEA-Gid2/RMND5A catalytic domain is conserved in all GID/CTLH orthologs we examined. The extent of the GID/CTLH E3 basic patch strikingly correlates with the length of its cognate Ubc8/UBE2H E2 C-terminal extension (Figure 7B).

Despite differing lengths, all C-terminal extensions feature distal φ-pSer-D/E motifs (φ denotes hydrophobic residue) (Figure 7B). Notably, this motif corresponds to the well-resolved regions in the cryo-EM maps, and thus may be instrumental for anchoring E2-E3 interactions.

DISCUSSION

With ≈40 E2s and ≈600 E3s mediating ubiquitylation in humans, it is important to understand how their pairing is established. In studying the dedicated partnership between

Ubc8/UBE2H-family E2s and GID/CTLH-family E3s, we unexpectedly found a plethora of unique interactions: (1) a catalytic assembly resembling but distinct from other RING-family E3 complexes with E2s; (2) elaborate GID/CTLH-specific interactions encasing Ubc8/UBE2H via a UBC domain surface typically not involved in E3-binding; and (3) complementary polyelectrostatic interactions between the E2 C-terminal extension and a large basic patch on the cognate E3. Notably, these latter interactions are potentiated by E2 multisite phosphorylation. Furthermore, our unbiased proteome-wide analysis revealed that mutation of the UBE2H phosphorylation sites exclusively impaired binding to the CTLH complex (Figure 3G). While it is possible that UBE2H C-terminus might contribute to interactions with other E3s, other known UBE2H partners such as MG53 (aka TRIM72)[63,64] were not detected in our assay as being impaired by the mutations. Therefore, our data support the role of phosphorylation in establishing this dedicated E2-E3 pair.

Discovery of Ubc8/UBE2H C-terminal phosphorylation emerged from the cryo-EM structures, as this region is invisible to standard phosphoproteomic techniques. This highlights the value of experimental approaches to structural biology. Meanwhile, resolving the structures by cryo-EM depended on homogeneity of the phosphorylation-dependent interactions. Indeed, seven neighboring UBE2H phosphoserines were observed engaging the CTLH E3 (Figure 6B), thus adding to a growing list of polyelectrostatic interactions involving E3 ligase basic patches and acidic sequences in their binding partners. For example, the basic patch on the E3 substrate receptor Cdc4 was shown to selectively recruit substrates phosphorylated on multiple sites[47,48], and cullin-RING ligase basic patches were found to recruit acidic tails from UBE2R-family E2s[45,46]. These previously reported interactions are polyelectrostatic and thus fluid in nature, with ongoing sampling of multiple distinct conformations. By contrast, at least the contacts between GID/CTLH E3s and multiphosphorylated Ubc8/UBE2H observed in our cryo-EM structures strikingly differ in their specific character. The defined anchoring point of the E2 phosphosites relative to the E3 catalytic domain seems critical to promote formation of an active E3-E2~ubiquitin assembly. Although the lengths of Ubc8/UBE2H C-terminal extensions differ in orthologs across evolution, they correlate with relative positions of GID/CTLH E3 basic patches. Thus, our work provides a refined view on such polyelectrostatic interactions, illuminating their capacity to form specific contacts to promote catalysis.

What might be advantages of such intricate pairing, considering that E3 RING and E2 UBC domains are often sufficient for ubiquitylation? First, from a regulatory perspective, the extreme specificity would determine timing of ubiquitylation, such that GID/CTLH E3 activity is tied to Ubc8/UBE2H levels. Notably, both yeast Ubc8 and human UBE2H expression are coordinated with their cognate GID/CTLH E3 subunits, both transcriptionally and post-transcriptionally[8,25–27,65]. Another function would be rigidifying the catalytic centers within a flexing E3-substrate complex. The Ubc8~ubiquitin-GID complex is conceptually reminiscent of a bungee trampoline, with Fbp1 flexibly tethered to both sides (Figure S2B). The fixed placement of the base of a trampoline – or here, the E3 RING-Ubc8~ubiquitin intermediate secured to the catalytic module – increases the chance of encounter with the tethered jumper, or substrate. As shown by channeling of Fbp1 to two constrained active sites (Figure 1, Video S1), this could be particularly important for ubiquitylation of folded substrates on multiple target lysines, much like multi-enzymatic assemblies transferring reaction intermediates between consecutive active sites without release into bulk solution[66]. Finally, the bipartite nature of the Ubc8/UBE2H-GID/CTLH assembly could impart processivity. Indeed, compared to its unphosphorylated counterpart, phosphorylated Ubc8 modifies more sites, and builds longer polyubiquitin chains in a single substrate binding event (Figure S3D). Considering phosphorylated E2s migrate with E3 even in the absence of conjugated ubiquitin on a non-denaturing gel (Figure 6E), it seems likely that Ubc8 and UBE2H remain tethered to GID/CTLH coiled-coils even after ubiquitin transfer. This would offer a means for recharging the liberated, yet flexibly tethered, UBC domain to recycle it for another round of ubiquitylation without the need of dissociating from the E3. Thus, the identified molecular principles not only illuminate an intimate E2-E3 partnership conserved across evolution, but also illustrate how crosstalk between two major post-translational modifications, phosphorylation and ubiquitylation, orchestrate an efficient multiprotein enzymatic machine.

Limitations of the Study

Although future studies will be required to determine whether the phosphorylation status of Ubc8/UBE2H is subject to regulation, evolutionary preservation of the phosphorylation-driven E2-E3 pairing mechanism suggests potential regulatory roles. Indeed, we demonstrated that a candidate kinase capable of targeting yeast Ubc8 and human UBE2H is CK2, which, despite being constitutively active, is implicated in a plethora of signaling pathways[67]. Further potential for regulation is indicated by our findings that Ubc8/UBE2H-GID/CTLH interactions are antagonized *in vitro* by dephosphorylation and vice-versa (Figures 5 and 6). We speculate that GID/CTLH-dependent cellular activities could be regulated by cycles of phosphorylation/dephosphorylation, akin to other biological systems regulated by reversible post-translational modifications, such as acetylation or neddylation[68,69].

Also, we note that cryo-EM best visualizes homogeneous interactions. Since the structural study of the yeast complex was performed with Ubc8 that was heterogeneously phosphorylated through expression in insect cells, it is conceivable that the fully phosphorylated version might make additional contacts. Moreover, as for most cryo-EM structures, the final high-resolution reconstructions of GID/CTLH catalytic assemblies were performed with relatively small subsets of particles that were more homogeneous. Thus, it is possible that they represent only the most stable arrangements of Ubc8/UBE2H C-terminal extensions. Nonetheless, the mutational data – not only *in vitro* but also *in vivo* – support a crucial role for the structurally observed phosphorylation-dependent interactions (Figure 4).

STAR METHODS

RESOURCE AVAILABILITY

Lead contact—Further information and requests for resources and reagents should be directed to and will be fulfilled by the lead contact, Prof. Dr. Brenda Schulman (schulman@biochem.mpg.de)

Materials availability—All unique/stable reagents generated in this study are listed in the key resources table and are available from the lead contact with a completed Materials Transfer Agreement.

Data and code availability

- Cryo-EM maps, masks, and structural coordinates have been deposited at the Research Collaboratory for Structural Bioinformatics (RCSB) and Electron Microscopy Data Bank (EMDB) and are publicly available as of the date of publication. Their accession codes are listed in the key resources table. Raw image data have been deposited at Mendeley and are publicly available as of the date of publication. The DOI is listed in the key resources table. The mass spectrometry proteomics data have been deposited at the ProteomeXchange Consortium via the PRIDE[88] partner repository and are also provided as Table S2. Their dataset identifier is listed in the key resources table.
- This paper does not report original code.
- Any additional information required to reanalyze the data reported in this paper is available from the lead contact upon request.

EXPERIMENTAL MODEL AND STUDY PARTICIPANT DETAILS

Cell lines

High Five Insect Cells: Cells were grown in EX-CELL 420 Serum-Free Medium at 27°C.

Flp-In-T-REx-HEK293 Human Cells (RRID: CVCL_U427): Cells were cultured in DMEM (GIBCO), supplemented with 10% (v/v) FBS (GIBCO), GlutaMAX (GIBCO), 100 units/ml penicillin, 0.1 mg/ml streptomycin, 0.1 mg/ml zeocin, and 15 μg/ml blasticidin S-HCl at 37°C and 7% CO_2.

Organisms/Strains:

E. coli BL21 RIL (DE3): Cells were grown in Terrific Broth (TB) medium at 37 or 18°C.

E. coli DH5α: Cells were grown in LB medium at 37°C.

S. cerevisiae: Yeasts were grown in SD-glucose or SE medium at 30°C.

METHOD DETAILS

Yeast strain construction—All the *S. cerevisiae* yeast strains used in this study were constructed as derivatives of BY4741 using standard genetic techniques[89–91] and verified by PCR, DNA sequencing and immunoblotting.

***In vivo* yeast substrate degradation assays—**To examine physiological relevance of Ubc8 phosphorylation (Figures 3J and S3G), complement the structural insights (Figures 4D and 4F), and query importance of CK2 for GID substrate turnover (Figure 5E), we performed *in vivo* degradation assays of Fbp1 or Mdh2 using the promoter reference technique[92]. Yeast strains (expressing WT or C-terminally Myc- or V5–8xHis-tagged

Ubc8 mutants – Figures 3J and 4D, respectively; WT or basic patch mutant 3xFLAG-Gid2 – Figure 4F; carrying individual deletions of *CKA1* and *CKA2* genes – Figure 5E; or expressing C-terminally Myc-tagged WT or mutant Ubc8 in the WT or Gid7 deletion background – Figure S3G) were first transformed with a plasmid harboring coding sequences of Fbp1 or Mdh2, and a reference protein DHFR (C-terminally 3xFLAG and HA-tagged, respectively) expressed from identical promoters. Cells were grown in SD-glucose medium (0.17% yeast nitrogen base, 0.5% ammonium sulfate, 2% glucose, amino acid mix) to OD_{600} of 1.0 and then starved in SE medium (0.17% yeast nitrogen base, 0.5% ammonium sulfate, 2% ethanol, amino acid mix) for 19 hours. Following ethanol starvation, the equivalent of 1 OD_{600} of cells was transferred back to SD-glucose medium containing 0.5 mM tetracycline to repress translation of plasmid-encoded proteins and initiate the recovery process. 1 OD_{600} of cells was harvested at various time points of glucose recovery.

The harvested cells were lysed by resuspending in 800 μL 0.2 M NaOH and incubating on ice for 20 minutes, with subsequent centrifugation at 11,200xg for 1 minute at 4°C. The obtained pellets were resuspended in 50 μL HU buffer (8 M Urea, 5% SDS, 1 mM EDTA, 100 mM DTT, 200 mM Tris-HCl pH 6.8, EDTA-free Complete protease inhibitor tablet (Roche), bromophenol blue), heated at 70°C for 10 minutes and then centrifuged again at 11,200xg for 5 minutes at 4°C. Levels of Fbp1 or Mdh2, and DHFR were visualized by immunoblotting with anti-FLAG (Sigma) and anti-HA (Sigma) antibodies, respectively, and imaged using a Typhoon scanner (GE Healthcare). Bands were quantified using the ImageStudioLite software (LI-COR). The signals for Fbp1 or Mdh2 were normalized to that of DHFR and plotted in PRISM v9.1.0 (GraphPad) relative to their normalized values at timepoint 0. For statistical analysis, at least three biological replicates were considered.

Plasmid preparation and mutagenesis—All genes used in this study were obtained as previously described[36,37], apart from that encoding human CK2α, which was obtained from human cDNA library (Max Planck Institute of Biochemistry). Constructs for protein expression were prepared using the Gibson assembly method[93], while their mutant versions were generated with the QuickChange protocol (Agilent). Genes encoding GID/CTLH subunits were combined into single baculoviral expression constructs by biGBac assembly[94]. All the coding sequences used for protein expression were verified by DNA sequencing.

Protein preparation

Insect cell expression and purification: High Five insect cells (ThermoFisher Scientific) were transfected with recombinant baculovirus variants harboring protein-coding sequences listed in the key resources table and grown for 72 hours in EX-CELL 420 Serum-Free Medium at 27°C. After harvesting, cell pellets were resuspended in the lysis buffer containing 50 mM Tris pH 8, 150 mM NaCl, protease inhibitors (10 μg/ml leupeptin, 20 μg/ml aprotinin, EDTA-free Complete protease inhibitor tablet (Roche, 1 tablet per 50 mL of buffer) and 1 mM PMSF) and 5 mM DTT. For resuspension of insect cells expressing E2s, the lysis buffer was additionally supplemented with phosphatase inhibitors 50 mM sodium fluoride (Sigma) and 50 mM β-glycerophosphate (Sigma) to suppress post-lysis dephosphorylation. The resuspended insect cells were disrupted by sonication and centrifuged to remove cell debris.

To purify WT and mutant versions of GID and CTLH E3s for cryo-EM and biochemistry, we appended a Twin-Strep tag at the C-terminus of Gid8 or its human homolog TWA1. The C-terminal Twin-Strep tag was also fused to insect cell-expressed Ubc8 and UBE2H variants that were used for qualitative ubiquitylation and binding assays. The cleared insect cell lysates were subjected to Strep-Tactin affinity (IBA-Lifesciences) and size exclusion chromatography (SEC) in the final buffer containing 25 mM HEPES pH 7.5, 150 mM NaCl and 1 mM (Buffer A) or 5 mM (Buffer B) DTT for biochemical assays and cryo-EM, respectively. For purification of Chelator-GID^{SR4}, the affinity-purified complex was additionally subjected to anion exchange chromatography prior to SEC. The CTLH E3 subcomplex used for Octet BLI experiments was additionally treated with Tobacco Etch Virus (TEV) protease at 4°C overnight to remove the Twin-Strep tag from TWA1 C-terminus. The digested samples were run on SEC in 25 mM HEPES pH 7.5, 150 mM NaCl and 2 mM TCEP.

WT and mutant IC Ubc8 and UBE2H used for kinetics and cryo-EM were expressed as N-terminal GST fusions. E2s were purified from insect cell lysates by glutathione affinity chromatography (Cytiva), followed by an overnight incubation with TEV protease at 4°C to liberate the GST tag. After anion exchange chromatography and SEC in Buffer A, the pooled fractions were passed back over the glutathione affinity resin to remove residual GST. The phosphorylation status of various IC E2 versions was determined by intact mass analysis performed in the MPIB Mass Spectrometry Core Facility.

ARMC8-specific VH[27] included in the cryo-EM sample of CTLH^{SR4}-UBE2H~ubiquitin was expressed with an N-terminal 6xHis tag and C-terminally fused UBE2H C-terminal extension (aa 151–183). After resuspension of the insect cell lysate in the buffer containing 50 mM Tris pH 8, 150 mM NaCl, 1 mM PMSF, 5 mM β-ME and 10 mM imidazole, it was purified by nickel affinity chromatography (Sigma).

Bacterial expression and purification: Codon-enhanced BL21 (DE3) pRIL *E. coli* cells were transformed with plasmids harboring protein-coding sequences as described in the key resources table. Protein expression was induced with 0.4 mM IPTG and carried out overnight at 18°C. After harvesting, cell pellets were resuspended in the lysis buffer containing 50 mM Tris pH 8, 150 mM NaCl, 1 mM PMSF and 5 mM DTT (for GST- and Twin-Strep-tagged proteins) or 5 mM β-ME and 10 mM imidazole (for 6xHis-tagged proteins).

The bacterially expressed versions of Ubc8 and UBE2H used for kinetic experiments as well as human GID4 (Δ1–99) were expressed as N-terminal GST-fusions, whereas GID substrates, Fbp1 and Mdh2, and ubiquitin used to prepare stable E2~ubiquitin mimics were expressed with a 6xHis-tag appended to their C- or N-termini, respectively. For qualitative ubiquitylation and binding assays, Ubc8 and UBE2H were C-terminally tagged with Twin-Strep. Proteins were purified by affinity chromatography and SEC as described for insect cell-expressed proteins. For GST-tagged E2s, proteins after overnight TEV cleavage were subjected to anion exchange chromatography before final SEC.

To obtain fully phosphorylated Ubc8 and UBE2H for biochemical assays, their GST-tagged versions were co-expressed with the catalytic subunit of CK2 (CK2α), which was shown to be active on its own, even in the absence of the regulatory subunit CK2β[95].

Untagged WT ubiquitin used for *in vitro* ubiquitylation assays was purified via glacial acetic acid method[71] followed by gravity cation exchange chromatography (GE Healthcare) and SEC in Buffer A.

Preparation of stable E2~ubiquitin mimics—To prepare stable mimics of E2~ubiquitin intermediates, we enzymatically conjugated the C-terminus of 6xHis-3C-ubiquitin (3C is the cleavage site for the HRV-3C protease) to the sidechains of lysine residues substituting catalytic cysteines of Ubc8 and UBE2H (C85K and C87K, respectively) via an isopeptide bond. The loading reaction consisted of 0.5 μM E1 UBA1, 100 μM Ubc8 or UBE2H, 300 μM 6xHis-3C-ubiquitin and the loading reaction buffer (25 mM Bis-Tris propane pH 9.5, 100 mM NaCl, 2.5 mM $MgCl_2$ and 1 mM ATP). After overnight incubation at 42°C, the reaction mixture was run on SEC in the 6xHis pull-down buffer (25 mM HEPES pH 7.5, 200 mM NaCl, 5 mM imidazole, 5 mM β-ME) to remove E1 and excess ubiquitin. E2~ubiquitin was separated from unreacted E2 by nickel affinity chromatography (by pulling on 6xHis tag fused to ubiquitin) and SEC in the final buffer B.

Fluorescent labeling of GID substrates—GID substrates Fbp1 and Mdh2 were C-terminally labeled with fluorescein (FAM) via the sortase A-mediated reaction[72]. Labeling was performed by mixing 50 μM substrate (C-terminally tagged with a sortag (LPETGG) followed by a 6xHis tag), 250 μM fluorescent peptide (GGGGGFYVK-FAM) and 50 μM sortase A in a reaction buffer (50 mM Tris-HCl pH 8, 150 mM NaCl and 10 mM $CaCl_2$) followed by a 30-minute incubation at room temperature. The reaction mixture was supplemented with 5 mM imidazole and passed back over nickel affinity resin to remove unreacted substrates (harboring an uncleaved 6xHis tag). The fluorescent substrates were further purified by SEC in buffer A.

Phos-tag SDS-PAGE—To determine phosphorylation status of WT and mutant Ubc8/UBE2H, we analyzed their migration in Phos-tag SDS-PAGE gels (Figures 3C, 3D, 5B, 5C and 6F), which we prepared with optimized concentrations of acrylamide and Phos-tag reagent to achieve optimal separation of phosphorylated and unphosphorylated E2s. Gels were poured according to the manufacturer's protocol and contained 10% (w/v) acrylamide/bis-acrylamide 29:1 (Carl Roth), 50 μM Phos-tag Acrylamide (FUJIFILM Wako Chemicals),100 μL $ZnCl_2$, 350 mM Bis-Tris pH 6.8, TEMED (100 μL/100 mL gel solution, Carl Roth) and 0.05% (w/v) APS (Sigma) in the resolving gel solution. The electrophoresis running buffer contained 100 mM Tris pH 7.8, 100 mM MOPS, 0.1% (w/v) SDS and 5 mM sodium bisulfite. Gels were run at 30 mA for 90 minutes and imaged by a fluorescent scan, Coomassie staining or immunobloting.

Native gel electrophoresis—Native PAGE gels for band shift assay in Figure 6E were poured manually and contained 4.5% (w/v) acrylamide/bis-acrylamide 29:1, 2% (v/v) glycerol, Tris-borate (TB) buffer (100 mM Tris, 100 mM boric acid), TEMED (75 µL/100 mL gel solution) and 0.04% (w/v) APS. Gels were first pre-run for 5 minutes at 200 V and then run at 130 V for 50 minutes at 4°C in the TB buffer.

To assay association of fully phosphorylated and dephosphorylated BODIPY-labeled UBE2H and UBE2H~ubiquitin with CTLH (WT or basic patch mutant, Figure 6E), we mixed them at 1:2 E2:CTLH ratio (at 0.5 µM E2 and 1 µM E3). After 10 minutes of incubation at room temperature, the samples were mixed with a non-denaturing PAGE loading buffer (5% (v/v) glycerol, 1xTB buffer, bromophenol blue) and run on native PAGE gels. Proteins were visualized by a fluorescent scan.

Fluorescent labeling of E2s—For detecting different E2 versions in the Phos-tag SDS-PAGE and native PAGE gels, we labeled them fluorescently by chemically conjugating BODIPY-maleimide (ThermoFisher Scientific) to cysteines introduced into solvent-exposed regions of their catalytic cysteine>lysine mutants (C85K/K133C Ubc8 and C87K/E135C UBE2H or UBE2H~ubiquitin). Labeling reactions were set up by mixing 200 µM E2s in the reaction buffer (25 mM HEPES pH 7.5, 150 mM NaCl, 2 mM TCEP, 2 mM EDTA) and 2 mM BODIPY-maleimide. The mixtures were incubated for 1 hour at room temperature, quenched with 5 mM DTT and desalted to get rid of excess BODIPY. Finally, the labeled E2s were run on SEC in buffer A.

CK2-mediated *in vitro* phosphorylation assays—*In vitro* phosphorylation of BODIPY-labeled Ubc8 and UBE2H (Figure 5C) was performed by incubating 0.4 µg E2s with 1 µL CK2 (NEB) in 10 µL reaction mixtures supplemented with 10x Protein Kinases (PK) buffer (provided in the kit), 5 mM ATP and 10 mM $MgCl_2$ for 1 hour at room temperature. E2s were separated with Phos-tag SDS-PAGE and visualized by a fluorescent scan. Similarly, unlabeled bacterially expressed E2s were phosphorylated overnight at RT and analyzed with intact mass spectrometry (Figure 5D).

λPP treatment of phosphorylated E2s—To fully dephosphorylate IC E2s for biochemical assays (Figures 3B, 3E, 3H, S3A, S3B and S3E), 10 µL E2s were treated with 1 µL λPP (NEB) in the 15 µL reaction supplemented with 10x Protein Metallophosphatase (PMP) buffer and 1 mM $MnCl_2$ included in the kit. Mixtures were incubated at room temperature for 1 hour and quenched with 10 mM sodium orthovanadate (NEB).

For assay testing susceptibility of fully phosphorylated BODIPY-labeled UBE2H and UBE2H~ubiquitin in their free or CTLH-bound form to λPP-mediated dephosphorylation (Figure 6F), we incubated 0.5 µM E2 with 1 µM CTLH (WT or basic patch mutant) in the reaction mixture supplemented with the PMP buffer and 1 mM $MnCl_2$ for 10 minutes at room temperature. Dephosphorylation reactions were initiated by addition of λPP (10-fold diluted in buffer B, 1 µL/10 µL reaction) and quenched at different time points by mixing with SDS-PAGE loading buffer. Quenched samples were separated by Phos-tag SDS-PAGE and visualized by a fluorescent scan.

Kinase inhibitor assay—Since the computationally predicted candidate kinases CK2, CK1 and GSK3 are essential *in vivo*, we examined their capacity to phosphorylate E2 C-terminal extensions by employing a semi-*in vitro* assay (Figure 5B). 0.4 µg BODIPY-labeled BC UBE2H and Ubc8 were incubated with 15 µg lysate of, respectively, HEK293 cells or glucose-starved yeast (grown for 18 hours in ethanol) supplemented with 5 mM ATP and 10 mM $MgCl_2$ overnight at room temperature. Before adding E2s, the lysates were treated separately or in combination with 50 µM kinase inhibitors Silmitasertib (CX-4945, Selleckchem), SML0795 (Sigma) and PZ0313 (Sigma) dissolved in DMSO to inhibit, respectively, CK2, CK1 and GSK3. Samples without kinase inhibitors contained the corresponding volume of DMSO. Lysates were run on Phos-tag SDS-PAGE, followed by a fluorescent scan of the gels to visualize E2 phosphorylation pattern.

Qualitative *in vitro* ubiquitylation assays—All qualitative ubiquitylation assays were performed at room temperature in a buffer containing 25 mM HEPES pH 7.5, 150 mM NaCl, 5 mM ATP and 10 mM $MgCl_2$. Samples at indicated time points were quenched by mixing an aliquot of the total reaction mixture with a reducing SDS-PAGE loading buffer. Ubiquitylation of FAM-labeled substrates was visualized by a fluorescent scan of SDS-PAGE gel using the Amersham Typhoon imager (GE Healthcare).

Assays with model peptide substrates: Due to a lack of biochemically validated substrates of human CTLH, its previous mechanistic studies relied on a model peptide substrate designed based on the cryo-EM structure of CTLH^{SR4} [27,37]. Thus, to directly compare the effects of examined mutations between the yeast and human systems, we performed the majority of qualitative ubiquitylation assays examining the functional roles of E2 phosphorylation (Figures 3H, 4B, 4E, 4G and S5D) or validating the mode of E2~ubiquitin binding and activation (Figures 2B, 2C, S7E and S7F) using the analogous reaction set-ups involving the minimal catalytically competent E3 forms, GID^{SR4}/CTLH^{SR4}, and model peptide substrates. The model peptides comprised an N-terminal Gid4 recognition sequence (Mdh2 degron PHSVTPSIE for GID^{SR4} or human GID4 recognition motif PGLWRS[41] for CTLH^{SR4}) connected to a single target lysine placed at position 27 with a flexible linker, enabling spanning the structurally observed distance between the substrate binding site and the catalytic center[36,37].

All reactions with peptide substrates were performed in the multi-turnover format. Assays with yeast GID were set up by mixing 0.2 µM E1 UBA1, 1 µM WT or mutant C-terminally Twin Strep-tagged Ubc8, 0.5 µM WT or mutant GID^{SR4}, 1 µM C-terminally FAM-labeled model peptide substrate and 20 µM ubiquitin (added last to initiate the reaction). Reactions probing activity of human orthologs were performed in a similar way but we used 1 µM C-terminally Twin Strep-tagged UBE2H, 0.5 µM CTLH E3 version lacking substrate receptor GID4 (RANBP9-TWA1-ARMC8-RMND5A-MAEA) and 1 µM bacterially expressed GID4 (Δ1−99). Low level of model peptide ubiquitylation in the absence of E2 in the assay with CTLH^{SR4} (Figure 3H) was due to trace amounts of endogenous insect cell UBE2H co-purified with recombinant human CTLH from insect cells (detected by mass spectrometry).

For reactions testing activity of Ubc8 and UBE2H phosphorylated by co-expression with CK2α in bacteria (Figure S5D), the E2s expressed as GST fusions were used (liberated from GST before IEX).

Assays with folded yeast substrates: To examine how E2 phosphorylation affects ubiquitylation of folded substrates, we performed assays with yeast GID and its genetically validated substrates. Moreover, since GID adopts a collection of assemblies, the assays were performed with both Mdh2 and Fbp1 substrates and their cognate GID E3 forms, $\mathrm{GID}^{\mathrm{SR4}}$ and its supramolecular assembly Chelator-$\mathrm{GID}^{\mathrm{SR4}}$. The multi-turnover reactions (Figure S3B) were set up by mixing 0.2 μM E1 UBA1, 1 μM Ubc8–2xS, 0.5 μM $\mathrm{GID}^{\mathrm{SR4}}$ or Chelator-$\mathrm{GID}^{\mathrm{SR4}}$, 1 μM Mdh2-FAM or Fbp1-FAM and 20 μM ubiquitin.

To examine differences in modification of Fbp1 and Mdh2 during a single E3 binding event (Figures S3C and S3D), we prepared two mixtures with the following concentrations in the final reaction mix: 1) E2~ubiquitin mix: 8 μM E2, 0.2 μM E1, 20 μM ubiquitin, 5 mM ATP, 10 mM $\mathrm{MgCl_2}$, unlabeled competitor: 400 μM Mdh2 degron peptide (PHSVTPSIEQDSLK) or 10 μM Mdh2–6xHis (with preferred target lysines K254, K256, K259, K330, K360, K361 mutated to arginines)[36] for reactions with Mdh2 and Fbp1, respectively; 2) E3-substrate mix: 1 μM $\mathrm{GID}^{\mathrm{SR4}}$ or 0.5 μM Chelator-$\mathrm{GID}^{\mathrm{SR4}}$, 0.1 μM Mdh2-FAM or Fbp1-FAM. After a 10-minute pre-incubation of the two mixtures at room temperature, they were combined to begin the reaction. Presence of an unlabeled competitor in Mix 1 discouraged re-binding of substrates and products upon their dissociation from E3. A ‘no encounter’ control was performed to test the efficiency of unlabeled competitors in blocking fluorescent substrate binding by including them in Mix 2. Single turnover reactions were set up in the same way but the unlabeled competitor was not included. The same set of assays was performed with ‘lysineless’ K0 ubiquitin (with all lysines mutated to arginines) that cannot form polyubiquitin chains to determine the number of ubiquitylation sites on the substrates.

E2~ubiquitin discharge assay—To test the influence of Ubc8/UBE2H phosphorylation on its intrinsic activity in the presence or absence of E3, we performed a substrate-independent assay monitoring discharge of ubiquitin from a preformed E2~ubiquitin to a free lysine nucleophile in solution (Figure S3E). First, E2s were loaded with ubiquitin in the pulse reaction by mixing 0.5 μM E1 UBA1, 10 μM E2 (WT or mutant Twin Strep-tagged Ubc8 or UBE2H), 30 μM ubiquitin, 2.5 mM $\mathrm{MgCl_2}$ and 1 mM ATP. After 30 minutes at room temperature, the loading reactions were quenched with 50 mM EDTA. Next, the chase was initiated by mixing an equal volume of the quenched pulse with the discharge-initiation mixture containing either 25 mM or 50 mM lysine pH 8.0 (for reaction with $\mathrm{GID}^{\mathrm{SR4}}$ and $\mathrm{CTLH}^{\mathrm{SR4}}$, respectively) and 0 or 1 μM E3. Discharge reactions were quenched at indicated time points by mixing with a non-reducing SDS-PAGE loading buffer. The progress of discharge reactions was visualized by Coomassie-stained SDS-PAGE. Bands corresponding to E2 and E2~ubiquitin were quantified using ImageStudioLite (LI-COR) as a ratio of remaining E2~ubiquitin and the total E2 amount, and plotted in PRISM v9.1.0 (GraphPad) relative to the time point 0. The assays were performed in duplicates.

E2-E3 qualitative binding assays—To qualitatively probe association of different Ubc8/UBE2H versions with GID/CTLH E3s, we performed pull-down assays using the

C-terminally Twin-Strep-tagged E2s and insect cell lysates expressing untagged E3s (Gid1-Gid5-Gid8-Gid2-Gid9 or RANBP9-ARMC8-TWA1-MAEA-RMND5A-WDR26-MKLN1) (Figure 3E) or bacterial lysates expressing untagged isolated catalytic modules (Gid2-Gid9 or RMND5A-MAEA) (Figure S3A). 100 µg WT or mutant E2 were incubated with 1 mL lysates for 30 minutes and mixed with 25 µL Strep-Tactin resin (IBA Lifesciences). After another 30 minutes, Strep-Tactin beads were thoroughly washed with Buffer A. Finally, proteins were eluted with 50 µL of 2xStrep-Tactin elution buffer and analyzed by Coomassie-stained SDS-PAGE. To control for non-specific binding of lysate components or untagged E3s to Strep-Tactin resin, we incubated it with the lysates in the absence of E2.

Octet BioLayer Interferometry—To quantify the effect of UBE2H phosphorylation on its interaction with the CTLH E3, we determined the equilibrium dissociation constant (K_D) by Octet BioLayer Interferometry (BLI) (Figures 3F and S4A). Briefly, GST fusions of UBE2H (at 0.2 µg/mL) were immobilized on the anti-GST biosensors, followed by E3 association and dissociation steps lasting for 360 and 250 s, respectively. A parallel set of measurements was performed with GST only-loaded biosensors to control for the non-specific binding of the CTLH E3. The reference response values were subtracted from those elicited by the corresponding biosensors loaded with GST-E2s.

All BLI experiments were carried out at 25°C using the Octet K2 machine (Sartorius). Before the assay, concentrated GST-E2s (BC, S,T>D and IC UBE2H) and CTLH E3 (a biochemically well-behaved CTLH E3 subcomplex containing the catalytic subunits, RMND5A-MAEA-TWA1-RANBP9) were diluted with the binding buffer (25 mM Hepes pH 7.5, 150 NaCl, 0.5 mM TCEP, 0.5 mg/mL BSA and 0.05 % Tween 20 in the final reaction mixture). The same buffer was used to prepare a 3-fold dilution series of E3. The raw data were processed with Octet Analysis software HT 11.1.0.25 (Sartorius). Extracted response wavelength shifts in the steady-state regions of association curves from three or more independent measurements were extracted and plotted in PRISM v9.1.0 (GraphPad). K_D was estimated by non-linear regression using the one-site binding model. E3 molarity was calculated assuming the 2xRANBP9:2xTWA1:1xRMND5A:1xMAEA stoichiometry, which is consistent with cryo-EM structures of the CTLH E3.

Pre-steady state kinetics—Pre-steady state enzyme kinetics was employed to estimate the effects of Ubc8 phosphorylation on E2-E3 affinity (K_m) and the rate of ubiquitin transfer to E3-bound substrate (k_{obs}). Experiments were performed under single encounter conditions (substrate for E3) that enabled estimation of K_m and k_{obs}. This was accomplished by the inclusion of unlabeled peptide shown to have affinity for the E3[44] that discourages reassociation of labeled substrate and/or products to E3 (see below). Reactions were performed with monomeric GID^{SR4} that contains a single substrate binding site and functions most optimally with the dimeric gluconeogenic substrate Mdh2 (modified to contain a single preferred lysine ubiquitin acceptor residue K330 per subunit, with all of its previously determined preferred target lysines[36] K254, K256, K259, K360, K361 apart from K330 mutated to arginines).

Estimation of K_m of Ubc8 for GID E3: Single-encounter ubiquitylation reactions for substrate and E3 (Figures 3I, 4C, S4B and S5E) were assembled at room temperature by preparing two mixtures. Mix 1 contained 1 μM GID^{SR4} and 0.2 μM Mdh2-FAM (K254/K256/K259/K360/K361R mutant). E3 and substrate were diluted in 1x reaction buffer (30 mM Tris-HCl pH 7.5, 100 mM NaCl, 5 mM $MgCl_2$, 2 mM DTT, and 2 mM ATP) and incubated for 15 minutes. Mix 2 contained 1 μM E1 UBA1, ubiquitin, and 20 μM unlabeled peptide competitor (Mdh2 N-terminus PHSVTPSIEQDSLK), which were diluted in 1x reaction buffer and incubated for 2 minutes before being equally aliquoted to nine fresh tubes. Next, a two-fold dilution series of Ubc8 was constructed as follows. For all insect cell-expressed Ubc8 and for the bacterially expressed phosphomimetic mutant (CTE S,T>D), a serial 2-fold dilution of 100 μM E2 stock was prepared in 1x reaction buffer (an exception was CTE S,T>A mutant, which started from 300 μM). For bacterially-expressed WT Ubc8, a 2-fold dilution series was prepared using a 400 μM E2 stock, whereas for that co-expressed with CK2α (BC + CK2), 85 μM stock was used. E2 loading was carried out by mixing each E2 solution with Mix 1 at 1:4 ratio, followed by a 15-minute incubation period. The concentration of ubiquitin in Mix 1 was calculated so that its final concentration in all loading reactions was 2-fold greater than the highest E2 concentration in the titration series. Single-turnover ubiquitylation reactions were initiated by mixing equal volumes of Mix 1 and Mix 2-E2 mixture. All reactions were quenched after 10 s with 2xSD-SPAGE buffer (100 mM Tris-HCl pH 6.8, 20% glycerol, 30 mM EDTA, 4% SDS, and 4% β-mercaptoethanol). Substrates and products were resolved on 12% SDS-PAGE gels and imaged by a fluorescent scan with an Amersham Typhoon 5 instrument. Quantification of substrates and products was performed using ImageQuant software (Cytiva), where the percent of products formed, defined as substrate that had been conjugated to one or more ubiquitins, was estimated by dividing the sum of signal for all products by that for substrate and products. The data were fit to the Michaelis-Menten equation using nonlinear regression in PRISM v9.1.0 (GraphPad).

Estimation of the rate of ubiquitin transfer k_{obs}: Similar to the assays for K_m determination, ubiquitylation reactions were prepared as single-encounter between substrate and E3 (Figures 3I, 4C, S4C and S5E). In Mix 1, 1 μM GID^{SR4} E3 and 0.2 μM Mdh2-FAM were diluted in 1x reaction buffer. Meanwhile, 1 μM E1, ubiquitin, Ubc8, and 20 μM unlabeled peptide competitor were assembled in Mix 2. For all insect cell-expressed Ubc8 versions and for the bacterially expressed phosphomimetic mutant (CTE S,T>D), the E2 and ubiquitin concentrations in Mix 2 were, respectively, 10 μM and 20 μM (an exception was CTE S,T>A Ubc8, for which 4-fold higher E2 and ubiquitin concentrations were used). For WT bacterially-expressed Ubc8, the E2 and ubiquitin concentrations were, respectively, 40 μM (or 20 μM for CK2-coexpressed one), and 80 μM. After a 15-minute incubation, Mix 1 and Mix 2 were sequentially loaded into sample loops of a KinTek RQF-3 quench flow instrument. The reactions were initiated at various time points by mixing these solutions using a drive buffer (30 mM Tris-HCl pH 7.5, and 100 mM NaCl) prior to quenching in 2xSDS-PAGE buffer. Substrate and products were resolved on 12% SDS-PAGE gels and imaged by a fluorescent scan. Quantification was performed using ImageQuant (Cytiva) as described above followed by fitting the data to closed-form solutions of the kinetic model[97] using Mathematica.

Cell biological experiments

Cell culture and transfection: Flip-In T-Rex-HEK293 (HEK293) obtained from ATCC (CRL-1573) were cultured in DMEM (GIBCO), supplemented with FBS (10% (v/v)) (GIBCO), GlutaMAX (GIBCO), penicillin (100 units/ml), streptomycin (0.1 mg/ml), Zeocin (100 μg/ml), and Blasticidin S HCl (15 μg/ml) (GIBCO) at 37°C in a humidified incubator at 7% CO_2. The cultures were frequently checked for the absence of mycoplasma contamination.

HEK293 cell lines with stably integrated WT or basic patch mutant 3xFLAG-MAEA were generated using the Flp-In system (Invitrogen). Expression of 3xFLAG-MAEA was induced with 1 μg/ml tetracycline overnight prior to performing the experiment. For the expression of the different 3xFLAG-UBE2H variants (C-terminal deletions and phosphorylation site mutants), HEK293 cells were transiently transfected with pcDNA5a-3xFLAG-UBE2H variant plasmids using polyethylenimine (PEI) transfection reagent, and incubated for 48 h to reach maximal UBE2H expression.

Cell lysate preparation, immunoprecipitation, and immunoblot analysis: To generate HEK293 cell lysates, cells grown on 10 or 15-cm dishes were washed twice with ice-cold 1xPBS, scraped off in the presence of the lysis buffer (40 mM HEPES pH 7.5, 120 mM NaCl, 1 mM EGTA, 0.5% NP40, 1 mM DTT, and Complete protease inhibitor mix (Roche)), and incubated on ice for 10 min. Cells were homogenized by pushing them ten times through a 23G syringe. The obtained lysates were cleared by centrifugation at 23,000xg for 30 min at 4°C, and protein concentration was determined by Micro BCA-Protein Assay (ThermoFisher Scientific).

For qualitative experiments testing interactions of WT and mutant 3xFLAG-UBE2H (Figure 4H) with endogenous CTLH as well as the ability of 3xFLAG-MAEA in the CTLH complex to co-purify endogenous UBE2H (Figure S7G), 1–3 mg total cell lysate was incubated with anti-FLAG affinity resin (Sigma) for 1 hour at 4°C, which was then extensively washed with the lysis buffer. Immunoprecipitated proteins were eluted by boiling in reducing SDS-PAGE sample buffer, separated by SDS-PAGE and subjected to immunoblotting using indicated antibodies.

To examine specificity of interactions mediated by the phosphorylated C-terminal extension of UBE2H in the cellular context, we analyzed proteins co-immunoprecipitated with WT 3xFLAG-UBE2H relative to its CTE S>A mutant with quantitative mass spectrometry (Figure 3G, Table S2). HEK293 cells were mock, or transiently transfected with WT or mutant 3xFLAG-UBE2H and lysed in the lysis buffer (40 mM HEPES pH 7.5, 120 mM NaCl, 1 mM EGTA, 0.5% NP40, HALT Protein & Phosphatase Inhibitor Cocktail (ThermoFisher Scientific), and Complete protease inhibitor mix (Roche)). 3xFLAG-tagged proteins were captured from 3 mg of cleared lysate with anti-FLAG affinity resin (Sigma) for 2 h at 4°C, washed four times with the lysis buffer, followed by two washes with detergent-free buffer (40 mM HEPES pH 7.5, 120 mM NaCl, 1 mM EGTA), and analyzed by mass spectrometry.

For immunoblot analyses, HEK293 lysates were boiled at 95°C for 5 min in the SDS-PAGE sample buffer and separated by SDS-PAGE. Proteins were visualized using primary antibodies indicated in the key resources table. Blots were developed using Clarity Western ECL Substrate (BioRad) and imaged using Amersham Imager 600 (GE Lifesciences).

Visualization of UBE2H phosphorylation: To visualize the phosphorylation status of UBE2H in human cells (Figure 3D), we run HEK293 lysates ectopically expressing WT or mutant 3xFLAG-UBE2H on a Phos-tag SDS-PAGE gel and analyzed it by anti-FLAG immunoblotting. After electrophoresis, Phos-tag gels were first washed with 10 mM EDTA in Trans-Blot buffer (25 mM Tris, 192 mM glycine, 0.05 % (w/v) SDS, 20% (v/v) methanol) (3×10 minutes) to remove zinc ions. Subsequently, proteins were transferred to a nitrocellulose membrane for 90 minutes at 100 kV using a cold Trans-Blot buffer containing 0.1% (w/v) SDS. The membranes were blocked in 3% (w/v) milk in TBST (10 mM Tris pH 8, 150 mM NaCl, 0.1% (w/v) Tween 20) and incubated with primary anti-FLAG and secondary HRP-conjugated antibodies. FLAG-tagged proteins were detected by chemiluminescence.

LC-MS analysis of UBE2H interactome

Sample preparation: To analyze the phosphorylation-dependent interactome of UBE2H in HEK293 cells, the proteins immunoprecipitated with 3xFLAG-UBE2H WT and CTE S>A mutant were subjected to quantitative mass-spectrometry analysis (Figure 3G). Alkylation and reduction were done using 10 mM Tris(2-carboxyethyl)phosphine (TCEP), 40 mM 2-Chloracetamide (CAA) and 100 mM Tris-HCL pH 8.5 in 1% (w/v) sodium deoxycholate (SDC) buffer at 45°C for 5 min. The digestion was done using a 1:1000 ratio of protein and trypsin (w/w) at 37°C overnight with agitation (1400 rpm) on an Eppendorf Thermomixer C. Next, peptides were desalted using SDB-RPS (Empore) StageTips. For that, a tenfold dilution of the samples was done using 1% trifluoroacetic acid (TFA) in isopropanol. Samples were then loaded onto StageTips. StageTips were washed once with 200 μL of 1% TFA in isopropanol and then twice with 0.2% TFA/2% acetonitrile (ACN). 60 μL of 80% ACN/1.25% NH_4OH were used for peptide elution. Peptides were then dried using a SpeedVac centrifuge (Concentrator Plus; Eppendorf) for 1 h at 30 °C and resuspended in 0.2% TFA/2% ACN. 200 ng of peptides were subjected to LC-MS/MS analysis.

Data-independent acquisition: Peptides were loaded on a 50 cm reversed-phase column (75 μm inner diameter, packed in-house with ReproSil-Pur C18-AQ 1.9 μm resin). Column temperature was maintained at 50°C using a homemade column oven. An EASY-nLC 1200 system (ThermoFisher Scientific) was connected online with a mass spectrometer (Orbitrap Exploris 480, ThermoFisher Scientific) via nano-electrospray source. Peptide separation was done using a binary buffer system consisting of buffer A (0.1% formic acid (FA)) and buffer B (80% ACN, 0.1% FA). The flow rate was set to 300 nL/min. Peptides were eluted using a 75 min gradient. Peptide elution started with 2% buffer B and increased to 35% within 60 min, 60% within 70 min, and finally to 90% within 71 min, until it remained constant for the remaining 4 min. We used an MS set-up as described before[96]. In brief, we used a data-independent acquisition (DIA) mode with a full scan range of 300–1650 m/z at 120,000 resolution, automatic gain control [23] of 3e6, a maximum injection time of 20 ms and a stepped higher-energy collision dissociation (HCD) (set to 25, 27.5, and 30). Each full scan was followed by 44 DIA scans, which were performed at a 30,000 resolution, an AGC of 1e6, and the maximum injection time set to 54 ms.

DIA data processing and bioinformatics analysis: DIA Raw files were processed using the library free search on DIA-NN[98] v1.8.1. The search was performed against a UniProt human reference proteome of canonical and isoform sequences. We used the default settings with the following exceptions. We included carbamidomethylation, oxidation of methionine, and N-terminal acetylation of proteins as modifications. We turned on FASTA digest for library free search and the Deep learning-based spectra, RTs, and IMs predictions. Furthermore, heuristic protein inference was activated. The bioinformatics analyses and visualization were done using Python v3.5.5 with the following packages: pandas 1.4.2, numpy 1.21.5, matplotlib 3.5.13, seaborn 0.11.2, statsmodels 0.13.5. First, protein intensities were log2-transformed. Data was then filtered for valid values in at least one experimental group. Missing values were imputed using a Gaussian distribution with a shift of 3 and a width of 0.3 standard deviations. Unpaired two-tailed student's t-test was performed to determine statistical significance. The Benjamini Hochberg method was used for multiple testing correction. The source data of the proteomics experiment is provided as Table S2 and deposited in ProteomeXchange.

Structure determination by cryo-EM

Sample preparation and Imaging: To visualize how multiphosphorylated Ubc8~ubiquitin and UBE2H~ubiquitin engage GID/CTLH E3s, the cryo-EM samples were prepared as follows:

- Chelator-GID^{SR4} – Fbp1 – Ubc8~ubiquitin

  SEC fractions corresponding to Chelator-GID^{SR4} were pooled and concentrated to 1.2 mg/mL, mixed with 5-fold molar excess each of a stable Ubc8~ubiquitin mimic (prepared using heterogeneously phosphorylated insect cell-expressed Ubc8) and Fbp1–6xHis, and incubated for 30 minutes on ice before grid preparation.

- VH-bound CTLH^{SR4} – UBE2H~ubiquitin

  To date, it was only possible to obtain a high-resolution map of the GID catalytic module by focused refinement of yeast Chelator-GID^{SR4} while encapsulating an oligomeric substrate, which partially constrains motion of the constituent modules relative to each other[37]. However, the lack of well-characterized substrates of the human CTLH E3 has made it challenging to visualize the catalytic assembly. Therefore, we pursued a cryo-EM study in the context of the minimal catalytically-competent version of the CTLH complex consisting of the subunits forming the substrate receptor-scaffolding module (RANBP9-TWA1-ARMC8-GID4) bound to an engineered VH and the catalytic module (RMND5A-MAEA) bound to the stable mimic of fully phosphorylated UBE2H~ubiquitin.

> To prepare the sample, the affinity-purified CTLH subcomplex (RANBP9 - TWA1–2xS ARMC8 - RMND5A - MAEA) and engineered ARMC8-specific VH were mixed with 5-fold molar excess of bacterially expressed GID4 (Δ1–99) and run on SEC using a Superose 6 Increase column. SEC fractions corresponding to VH-bound CTLH^{SR4} were pooled, concentrated to 1 mg/mL, and incubated with 5-fold molar excess of UBE2H~ubiquitin (fully phosphorylated by treatment of ubiquitin-conjugated IC UBE2H with CK2 as described above) for 30 minutes on ice before grid preparation.

Cryo-EM grids were prepared using Vitrobot Mark IV (ThermoFisher Scientific) at 4°C and 100% humidity. 3.5 µl of protein samples were applied to glow-discharged holey carbon grids (R1.2/1.3, Cu 200 mesh, Quantifoil). Grids were blotted with Whatman no. 1 filter paper (blot time: 3 s, blot force: 3) and vitrified by plunging into liquid ethane.

Grids were first screened on either a Talos Arctica or Glacios transmission electron microscope (ThermoFisher Scientific) operated at 200 kV, equipped with a Falcon III (ThermoFisher Scientific) or K2 (Gatan) direct electron detector, respectively. The high-resolution datasets were collected on a Titan Krios microscope (ThermoFisher Scientific) operated at 300 kV, equipped with a post-column GIF and a K3 Summit direct electron detector (Gatan) operating in a counting mode. SerialEM v3.8.0-b5[74] (for Glacios and Titan Krios datasets) or EPU v2.7.0 (ThermoFisher Scientific, for Arctica dataset) software was used for automated data collection. Details of cryo-EM data collection and map refinement are listed in Table S1.

Data processing: Frames were motion-corrected with dose weighting using MotionCor2 v1.1[75] and subjected to estimation of contrast transfer function parameters with Gctf v1.06[76] integrated in Relion v4.0[77,78] or Focus software[73], which was used for on-the-fly pre-processing of Titan Krios data, while also automatically discarding poor quality images. Particles were automatically picked with Gautomatch v0.56 (K. Zhang, MRC Laboratory of Molecular Biology, Cambridge, UK) using a previously published map (EMD-12557) or a map from low-resolution datasets as templates for yeast and human datasets, respectively. All the subsequent stages of data processing were carried out with Relion v4.0. To clean up the data, while preserving rare views, extracted particles were subjected directly to 3D classification[99].

To reveal conformational dynamics of Chelator-GID^{SR4}-Fbp1-Ubc8~ubiquitin catalytic assembly, a clean set of particles was further 3D classified into 10 classes, out of which 5 were of high quality and contained all components of the ubiquitylation reaction (Figures S1A and S2A, Table S1). The chosen subsets of particles were subjected to masked autorefinement. The obtained maps were aligned and fit with previously published models in UCSF Chimera v.1.13.1[80], and analyzed by scanning across the collection of their still images as frames in a movie (Supplementary Video).

Owing to inherent flexibility of Chelator-GID^{SR4}, high-resolution reconstructions of its relatively rigid modules require a series of focused refinements[37]. Moreover, a two-fold symmetry (C2) of Chelator-GID^{SR4} enables doubling a particle number during refinement.

After cleaning up the initial set of particles, we performed auto-refinement with C2 symmetry imposed and generated masks around two opposing SRS-Cat-Ubc8~ubiquitin modules (Figure S1B, Table S1). Each mask was separately used for signal subtraction yielding two particle pools, which were combined and aligned by auto-refinement. After masking out the SRS module, multiple rounds of focused refinement and 3D classification without particle alignment with increasing T parameter were performed to enrich for particles having the most complete and well-resolved features. Final focused refinement was preceded by CTF refinement.

The overall map of human CTLH^{SR4} in complex with engineered VH and UBE2H~ubiquitin revealed two VH-bound SRS modules sandwiching the catalytic module in opposite orientations, which match their arrangement observed in the previous map of the WDR26-mediated CTLH E3 supramolecular assembly (EMD-12542)[37]. Similar to the yeast complex, the mobility between modules precludes refining the entire assembly to high resolution. Therefore, after performing auto-refinement over the entire complex with a clean set of particles, we progressively masked out both SRS modules, and performed a focused refinement around the UBE2H~bound catalytic module, followed by 3D classification without particle alignment (Figure S6). To enrich for particles containing UBE2H~ubiquitin, we performed two rounds of focused 3D classification (no alignment) with masks around RING-U-box RMND5A-MAEA catalytic domains and ubiquitin-conjugated UBE2H's UBC as well as the phosphorylated UBE2H C-terminal extension and the interacting part of the RMND5A-MAEA coiled-coil. After re-extracting the particles at full pixel size, the less well-resolved CTLH-CRA^{N} portion of RMND5A was masked out. Ultimately, the particles were subjected to several rounds of CTF refinement and Bayesian polishing, followed by final focused refinement.

All maps were post-processed by B-factor sharpening and high-resolution noise substitution in Relion v4.0. In addition, to aid in building atomic models, the refined high-resolution maps were sharpened with DeepEMhancer[79] (employing the highRes model), which are deposited as additional maps in EMDB. The estimated resolutions of all reconstructions are based on the gold-standard Fourier Shell Correlation (FSC) at 0.143 cut-off. Simplified flow charts of cryo-EM data processing are presented in Figures S1 and S6.

Model building and refinement: Manual building of models was performed with Coot v0.9.8.7[82,83], whereas structure visualization and analysis was carried out with UCSF Chimera v.1.13.1[80], UCSF ChimeraX v1.5[81] and PyMOL v2.5.2 (Schrödinger). Parameters of built models are listed in Table S1.

To obtain the model of the GID catalytic module bound to Ubc8~ubiquitin, we first docked the previous structure of Gid2-Gid9 (PDB 7NS4) into the post-processed map and manually refined or *de novo* traced differing or previously invisible parts, e. g. parts of the Gid2 RING and CRA^{C} that gets rearranged or ordered upon Ubc8~ubiquitin binding. Similarly, we docked the coordinates of AlphaFold2 prediction model of Ubc8's UBC and crystal structure of ubiquitin (PDB 1UBQ), which were then manually refined. Of note, we observed a clear density for engineered isopeptide bond between the very C-terminus of ubiquitin and the lysine substitution for Ubc8's catalytic cysteine (C85K mutation). To assign coordinates for the high-resolution portion of the phosphorylated Ubc8 C-terminal extension, we used positions of the hydrophobic residues as markers, considering that the visualized region is located in the distal portion of Ubc8 based on the lower resolution map resolving its entire C-terminus (Figure 2E). This supported placing sidechains of phosphoserines 202 and 207 in the additional globular densities unaccounted for by serine sidechains. The obtained model was validated by a mutational study (Figure 4).

The structure of human catalytic module in complex with UBE2H~ubiquitin was obtained by first fitting segments of AlphaFold2 prediction model for RMND5A-MAEA into electron density, followed by manual rebuilding of differing parts. Subsequently, crystal structures of UBE2H's UBC domain and ubiquitin (PDBs 2Z5D and 1UBQ) were docked and manually refined. As in the yeast structure, the isopeptide bond between ubiquitin C-terminus and UBE2H C87K was supported by clear electron density. Notably, despite the repetitive sequence of the phosphorylated part of UBE2H C-terminal extension, we could unambiguously assign and place sidechains of phosphoserines 168, 169, 171 and 174 owing to two hydrophobics M170 and F173 that punctuate the acidic stretch and strong electron density in this region. Placing of sidechains for three less well-resolved upstream phosphoserines 164, 165 and 166 was assisted by the map sharpened with DeepEMhancer.

Both yeast and human models were subjected to iterative rounds of manual building and real space refinement in PHENIX v1.19.2[84] until a satisfactory model quality, in terms of its geometry and agreement with the map, was achieved. Configurations of the zinc-binding sites within Gid2/RMND5A-Gid9/MAEA assembly and that of the isopeptide bond between ubiquitin and Ubc8/UBE2H C>K mutant were restrained during real-space refinement.

Structural superpositions—For structural analysis of Gid2 RING domain (Figure S2C), we superimposed its cryo-EM structure on that of LNX1 RING (PDB 5H7S)[100] and Siz1 SP-RING (PDB 5JNE)[56]. To analyze the closed activated conformation adopted by GID E3-bound Ubc8~ubiquitin (Figure S2E), we overlayed it with previous models of E2~ubiquitin (PDB 4AP4[52], 4V3L[101], 6SQS[102], 5MNJ [53], 7MEX [5], 3ZNI[103], 6HPR[104]) or E2~Ubls (PDB 4P5O[58] and 5JNE[56]) in complex with their cognate E3s.

QUANTIFICATION AND STATISTICAL ANALYSIS

For *in vivo* yeast substrate degradation assays, the levels of substrates (Fbp1–3xFLAG and Mdh2–3xFLAG) as well as the reference protein DHFR-HA were visualized by immunobloting and quantified using ImageStudioLite software (LI-COR). For statistical analysis, at least three biological replicates were considered.

For determining kinetic parameters of substrate ubiquitylation, intensities of fluorescently labeled Mdh2-FAM and its ubiquitylated versions in fluorescent scans of SDS-PAGE gels were quantified with ImageQuant (Cytiva). To analyze the substrate-independent ubiquitin discharge assay, intensities of E2 and E2~ubiqutin in Coomassie-stained gels were quantified with ImageStudioLite (LI-COR). For K_D determination, the steady-state responses from the BLI experiment were plotted in PRISM v9.1.0 (GraphPad) and analyzed by non-linear regression. All *in vitro* assays were performed in at least duplicates. The statistical parameters reported in the figures are described in the corresponding figure legends.

Supplementary Material

Refer to Web version on PubMed Central for supplementary material.

ACKNOWLEDGMENTS

We thank S. Übel and S. Pettera from MPIB Bioorganic Chemistry & Biophysics Core Facility for peptide synthesis, D. Bollschweiler and T. Schäfer for cryo-EM assistance, MPIB Mass Spectrometry Core Facility for intact mass analyses, and members of the Schulman lab for advice and support. This study was supported by the Max Planck Gesellschaft, the European Union (ERC, UPSmeetMet, 101098161), Leibniz Prize from the Deutsche Forschungsgemeinschaft (DFG, SCHU 3196/1) and NIH R01GM141409.

REFERENCES

1. Deshaies RJ, and Joazeiro CA. (2009). RING domain E3 ubiquitin ligases. Annu Rev Biochem 78, 399–434. 10.1146/annurev.biochem.78.101807.093809. [PubMed: 19489725]
2. Cappadocia L, and Lima CD. (2018). Ubiquitin-like Protein Conjugation: Structures, Chemistry, and Mechanism. Chem Rev 118, 889–918. 10.1021/acs.chemrev.6b00737. [PubMed: 28234446]
3. Metzger MB, Pruneda JN, Klevit RE, and Weissman AM. (2014). RING-type E3 ligases: master manipulators of E2 ubiquitin-conjugating enzymes and ubiquitination. Biochim Biophys Acta 1843, 47–60. 10.1016/j.bbamcr.2013.05.026. [PubMed: 23747565]
4. Baek K, Krist DT, Prabu JR, Hill S, Klugel M, Neumaier LM, von Gronau S, Kleiger G, and Schulman BA. (2020). NEDD8 nucleates a multivalent cullin-RINGUBE2D ubiquitin ligation assembly. Nature 578, 461–466. 10.1038/s41586-020-2000y. [PubMed: 32051583]
5. Pan M, Zheng Q, Wang T, Liang L, Mao J, Zuo C, Ding R, Ai H, Xie Y, Si D, et al. (2021). Structural insights into Ubr1-mediated N-degron polyubiquitination. Nature 600, 334–338. 10.1038/s41586-021-04097-8. [PubMed: 34789879]
6. Hammerle M, Bauer J, Rose M, Szallies A, Thumm M, Dusterhus S, Mecke D, Entian KD, and Wolf DH. (1998). Proteins of newly isolated mutants and the amino-terminal proline are essential for ubiquitin-proteasome-catalyzed catabolite degradation of fructose-1,6-bisphosphatase of Saccharomyces cerevisiae. J Biol Chem 273, 25000–25005. 10.1074/jbc.273.39.25000. [PubMed: 9737955]
7. Regelmann J, Schule T, Josupeit FS, Horak J, Rose M, Entian KD, Thumm M, and Wolf DH. (2003). Catabolite degradation of fructose-1,6-bisphosphatase in the yeast Saccharomyces cerevisiae: a genome-wide screen identifies eight novel GID genes and indicates the existence of two degradation pathways. Mol Biol Cell 14, 1652–1663. 10.1091/mbc.e02-08-0456. [PubMed: 12686616]
8. Schule T, Rose M, Entian KD, Thumm M, and Wolf DH. (2000). Ubc8p functions in catabolite degradation of fructose-1, 6-bisphosphatase in yeast. EMBO J 19, 2161–2167. 10.1093/emboj/19.10.2161. [PubMed: 10811607]
9. Menssen R, Schweiggert J, Schreiner J, Kusevic D, Reuther J, Braun B, and Wolf DH. (2012). Exploring the topology of the Gid complex, the E3 ubiquitin ligase involved in catabolite-induced degradation of gluconeogenic enzymes. J Biol Chem 287, 25602–25614. 10.1074/jbc.M112.363762. [PubMed: 22645139]
10. Santt O, Pfirrmann T, Braun B, Juretschke J, Kimmig P, Scheel H, Hofmann K, Thumm M, and Wolf DH. (2008). The yeast GID complex, a novel ubiquitin ligase (E3) involved in the regulation of carbohydrate metabolism. Mol Biol Cell 19, 3323–3333. 10.1091/mbc.E08-03-0328. [PubMed: 18508925]
11. Kong KE, Fischer B, Meurer M, Kats I, Li Z, Ruhle F, Barry JD, Kirrmaier D, Chevyreva V, San Luis BJ, et al. (2021). Timer-based proteomic profiling of the ubiquitin-proteasome system

reveals a substrate receptor of the GID ubiquitin ligase. Mol Cell 81, 2460–2476 e2411. 10.1016/j.molcel.2021.04.018. [PubMed: 33974913]

12. Langlois CR, Beier V, Karayel O, Chrustowicz J, Sherpa D, Mann M, and Schulman BA. (2022). A GID E3 ligase assembly ubiquitinates an Rsp5 E3 adaptor and regulates plasma membrane transporters. EMBO Rep 23, e53835. 10.15252/embr.202153835.
13. Zavortink M, Rutt LN, Dzitoyeva S, Henriksen JC, Barrington C, Bilodeau DY, Wang M, Chen XXL, and Rissland OS. (2020). The E2 Marie Kondo and the CTLH E3 ligase clear deposited RNA binding proteins during the maternal-to-zygotic transition. Elife 9. 10.7554/eLife.53889.
14. Cao WX, Kabelitz S, Gupta M, Yeung E, Lin S, Rammelt C, Ihling C, Pekovic F, Low TCH, Siddiqui NU, et al. (2020). Precise Temporal Regulation of Post-transcriptional Repressors Is Required for an Orderly Drosophila Maternal-toZygotic Transition. Cell Rep 31, 107783. 10.1016/j.celrep.2020.107783.
15. Maitland MER, Lajoie GA, Shaw GS, and Schild-Poulter C. (2022). Structural and Functional Insights into GID/CTLH E3 Ligase Complexes. Int J Mol Sci 23. 10.3390/ijms23115863.
16. Liu H, and Pfirrmann T. (2019). The Gid-complex: an emerging player in the ubiquitin ligase league. Biol Chem 400, 1429–1441. 10.1515/hsz-2019-0139. [PubMed: 30893051]
17. Lampert F, Stafa D, Goga A, Soste MV, Gilberto S, Olieric N, Picotti P, Stoffel M, and Peter M. (2018). The multi-subunit GID/CTLH E3 ubiquitin ligase promotes cell proliferation and targets the transcription factor Hbp1 for degradation. Elife 7. 10.7554/eLife.35528.
18. Lu Y, Xie S, Zhang W, Zhang C, Gao C, Sun Q, Cai Y, Xu Z, Xiao M, Xu Y, et al. (2017). Twa1/Gid8 is a beta-catenin nuclear retention factor in Wnt signaling and colorectal tumorigenesis. Cell Res 27, 1422–1440. 10.1038/cr.2017.107. [PubMed: 28829046]
19. Liu H, Ding J, Kohnlein K, Urban N, Ori A, Villavicencio-Lorini P, Walentek P, Klotz LO, Hollemann T, and Pfirrmann T. (2020). The GID ubiquitin ligase complex is a regulator of AMPK activity and organismal lifespan. Autophagy 16, 1618–1634. 10.1080/15548627.2019.1695399. [PubMed: 31795790]
20. Leal-Esteban LC, Rothe B, Fortier S, Isenschmid M, and Constam DB. (2018). Role of Bicaudal C1 in renal gluconeogenesis and its novel interaction with the CTLH complex. PLoS Genet 14, e1007487. 10.1371/journal.pgen.1007487.
21. Hantel F, Liu H, Fechtner L, Neuhaus H, Ding J, Arlt D, Walentek P, Villavicencio-Lorini P, Gerhardt C, Hollemann T, and Pfirrmann T. (2022). Cilia-localized GID/CTLH ubiquitin ligase complex regulates protein homeostasis of sonic hedgehog signaling components. J Cell Sci 135. 10.1242/jcs.259209.
22. Maitland MER, Kuljanin M, Wang X, Lajoie GA, and Schild-Poulter C. (2021). Proteomic analysis of ubiquitination substrates reveals a CTLH E3 ligase complex-dependent regulation of glycolysis. FASEB J 35, e21825. 10.1096/fj.202100664R.
23. Bagci H, Winkler M, Uliana F, Boulais J, Mohamed WI, Park SL, Côté J-F, and Peter M. (2023). The hGIDGID4 E3 ubiquitin ligase complex targets ARHGAP11A to regulate cell migration. bioRxiv, 2023.2007.2020.549906. 10.1101/2023.07.20.549906.
24. Zhen R, Moo C, Zhao Z, Chen M, Feng H, Zheng X, Zhang L, Shi J, and Chen C. (2020). Wdr26 regulates nuclear condensation in developing erythroblasts. Blood 135, 208–219. 10.1182/blood.2019002165. [PubMed: 31945154]
25. Lausen J, Pless O, Leonard F, Kuvardina ON, Koch B, and Leutz A. (2010). Targets of the Tal1 transcription factor in erythrocytes: E2 ubiquitin conjugase regulation by Tal1. J Biol Chem 285, 5338–5346. 10.1074/jbc.M109.030296. [PubMed: 20028976]
26. Nguyen AT, Prado MA, Schmidt PJ, Sendamarai AK, Wilson-Grady JT, Min M, Campagna DR, Tian G, Shi Y, Dederer V, et al. (2017). UBE2O remodels the proteome during terminal erythroid differentiation. Science 357. 10.1126/science.aan0218.
27. Sherpa D, Mueller J, Karayel O, Xu P, Yao Y, Chrustowicz J, Gottemukkala KV, Baumann C, Gross A, Czarnecki O, et al. (2022). Modular UBE2H-CTLH E2-E3 complexes regulate erythroid maturation. Elife 11. 10.7554/eLife.77937.
28. Soni S, Bala S, Gwynn B, Sahr KE, Peters LL, and Hanspal M. (2006). Absence of erythroblast macrophage protein (Emp) leads to failure of erythroblast nuclear extrusion. J Biol Chem 281, 20181–20189. 10.1074/jbc.M603226200. [PubMed: 16707498]

29. Wei Q, Pinho S, Dong S, Pierce H, Li H, Nakahara F, Xu J, Xu C, Boulais PE, Zhang D, et al. (2021). MAEA is an E3 ubiquitin ligase promoting autophagy and maintenance of haematopoietic stem cells. Nat Commun 12, 2522. 10.1038/s41467-021-22749-1. [PubMed: 33947846]
30. Pfirrmann T, Villavicencio-Lorini P, Subudhi AK, Menssen R, Wolf DH, and Hollemann T. (2015). RMND5 from Xenopus laevis is an E3 ubiquitin-ligase and functions in early embryonic forebrain development. PLoS One 10, e0120342. 10.1371/journal.pone.0120342.
31. Shin U, Choi Y, Ko HS, Myung K, Lee S, Cheon CK, and Lee Y. (2023). A heterozygous mutation in UBE2H in a patient with developmental delay leads to an aberrant brain development in zebrafish. Hum Genomics 17, 44. 10.1186/s40246-023-00491-7. [PubMed: 37208785]
32. Vourc'h P, Martin I, Bonnet-Brilhault F, Marouillat S, Barthelemy C, Pierre Muh J, and Andres C. (2003). Mutation screening and association study of the UBE2H gene on chromosome 7q32 in autistic disorder. Psychiatr Genet 13, 221–225. 10.1097/00041444-200312000-00005. [PubMed: 14639049]
33. Chana CK, Maisonneuve P, Posternak G, Grinberg NGA, Poirson J, Ona SM, Ceccarelli DF, Mader P, St-Cyr DJ, Pau V, et al. (2022). Discovery and Structural Characterization of Small Molecule Binders of the Human CTLH E3 Ligase Subunit GID4. J Med Chem 65, 12725–12746. 10.1021/acs.jmedchem.2c00509. [PubMed: 36117290]
34. Owens DDG, Maitland MER, Yazdi AK, Song X, Schwalm MP, Machado RAC, Bauer N, Wang X, Szewczyk MM, Dong C, et al. (2023). A chemical probe to modulate human GID4 Pro/N-degron interactions. bioRxiv, 2023.2001.2017.524225. 10.1101/2023.01.17.524225.
35. Serebrenik YV, Mani D, Maujean T, Burslem GM, and Shalem O. (2023). Pooled endogenous protein tagging and recruitment for scalable discovery of effectors for induced proximity therapeutics. bioRxiv, 2023.2007.2013.548759. 10.1101/2023.07.13.548759.
36. Qiao S, Langlois CR, Chrustowicz J, Sherpa D, Karayel O, Hansen FM, Beier V, von Gronau S, Bollschweiler D, Schafer T, et al. (2020). Interconversion between Anticipatory and Active GID E3 Ubiquitin Ligase Conformations via Metabolically Driven Substrate Receptor Assembly. Mol Cell 77, 150–163 e159. 10.1016/j.molcel.2019.10.009. [PubMed: 31708416]
37. Sherpa D, Chrustowicz J, Qiao S, Langlois CR, Hehl LA, Gottemukkala KV, Hansen FM, Karayel O, von Gronau S, Prabu JR, et al. (2021). GID E3 ligase supramolecular chelate assembly configures multipronged ubiquitin targeting of an oligomeric metabolic enzyme. Mol Cell 81, 2445–2459 e2413. 10.1016/j.molcel.2021.03.025. [PubMed: 33905682]
38. Mohamed WI, Park SL, Rabl J, Leitner A, Boehringer D, and Peter M. (2021). The human GID complex engages two independent modules for substrate recruitment. EMBO Rep, e52981. 10.15252/embr.202152981.
39. Melnykov A, Chen SJ, and Varshavsky A. (2019). Gid10 as an alternative Nrecognin of the Pro/N-degron pathway. Proc Natl Acad Sci U S A 116, 15914–15923. 10.1073/pnas.1908304116. [PubMed: 31337681]
40. Chen SJ, Wu X, Wadas B, Oh JH, and Varshavsky A. (2017). An N-end rule pathway that recognizes proline and destroys gluconeogenic enzymes. Science 355. 10.1126/science.aal3655.
41. Dong C, Zhang H, Li L, Tempel W, Loppnau P, and Min J. (2018). Molecular basis of GID4-mediated recognition of degrons for the Pro/N-end rule pathway. Nat Chem Biol 14, 466–473. 10.1038/s41589-018-0036-1.
42. Sherpa D, Chrustowicz J, and Schulman BA. (2022). How the ends signal the end: Regulation by E3 ubiquitin ligases recognizing protein termini. Mol Cell 82, 1424–1438. 10.1016/j.molcel.2022.02.004. [PubMed: 35247307]
43. Timms RT, and Koren I. (2020). Tying up loose ends: the N-degron and C-degron pathways of protein degradation. Biochem Soc Trans 48, 1557–1567. 10.1042/BST20191094. [PubMed: 32627813]
44. Chrustowicz J, Sherpa D, Teyra J, Siong Loke M, Popowicz G, Basquin J, Sattler M, Rajan Prabu J, Sidhu SS, and Schulman BA. (2021). Multifaceted N-degron recognition and ubiquitylation by GID/CTLH E3 ligases. J Mol Biol, 167347. 10.1016/j.jmb.2021.167347.
45. Sandoval D, Hill S, Ziemba A, Lewis S, Kuhlman B, and Kleiger G. (2015). Ubiquitin-conjugating enzyme Cdc34 and ubiquitin ligase Skp1-cullin-F-box ligase (SCF) interact through multiple conformations. J Biol Chem 290, 1106–1118. 10.1074/jbc.M114.615559. [PubMed: 25425648]

46. Kleiger G, Saha A, Lewis S, Kuhlman B, and Deshaies RJ. (2009). Rapid E2-E3 assembly and disassembly enable processive ubiquitylation of cullin-RING ubiquitin ligase substrates. Cell 139, 957–968. 10.1016/j.cell.2009.10.030. [PubMed: 19945379]

47. Mittag T, Orlicky S, Choy WY, Tang X, Lin H, Sicheri F, Kay LE, Tyers M, and Forman-Kay JD. (2008). Dynamic equilibrium engagement of a polyvalent ligand with a single-site receptor. Proc Natl Acad Sci U S A 105, 17772–17777. 10.1073/pnas.0809222105. [PubMed: 19008353]

48. Mittag T, Marsh J, Grishaev A, Orlicky S, Lin H, Sicheri F, Tyers M, and Forman-Kay JD. (2010). Structure/function implications in a dynamic complex of the intrinsically disordered Sic1 with the Cdc4 subunit of an SCF ubiquitin ligase. Structure 18, 494–506. 10.1016/j.str.2010.01.020. [PubMed: 20399186]

49. Baek K, Scott DC, and Schulman BA. (2021). NEDD8 and ubiquitin ligation by cullin-RING E3 ligases. Curr Opin Struct Biol 67, 101–109. 10.1016/j.sbi.2020.10.007. [PubMed: 33160249]

50. Watson ER, Brown NG, Peters JM, Stark H, and Schulman BA. (2019). Posing the APC/C E3 Ubiquitin Ligase to Orchestrate Cell Division. Trends Cell Biol 29, 117–134. 10.1016/j.tcb.2018.09.007. [PubMed: 30482618]

51. Alfieri C, Zhang S, and Barford D. (2017). Visualizing the complex functions and mechanisms of the anaphase promoting complex/cyclosome (APC/C). Open Biol 7. 10.1098/rsob.170204.

52. Plechanovova A, Jaffray EG, Tatham MH, Naismith JH, and Hay RT. (2012). Structure of a RING E3 ligase and ubiquitin-loaded E2 primed for catalysis. Nature 489, 115–120. 10.1038/nature11376. [PubMed: 22842904]

53. Nomura K, Klejnot M, Kowalczyk D, Hock AK, Sibbet GJ, Vousden KH, and Huang DT. (2017). Structural analysis of MDM2 RING separates degradation from regulation of p53 transcription activity. Nat Struct Mol Biol 24, 578–587. 10.1038/nsmb.3414. [PubMed: 28553961]

54. Dou H, Buetow L, Sibbet GJ, Cameron K, and Huang DT. (2012). BIRC7-E2 ubiquitin conjugate structure reveals the mechanism of ubiquitin transfer by a RING dimer. Nat Struct Mol Biol 19, 876–883. 10.1038/nsmb.2379. [PubMed: 22902369]

55. Pruneda JN, Littlefield PJ, Soss SE, Nordquist KA, Chazin WJ, Brzovic PS, and Klevit RE. (2012). Structure of an E3:E2~Ub complex reveals an allosteric mechanism shared among RING/U-box ligases. Mol Cell 47, 933–942. 10.1016/j.molcel.2012.07.001. [PubMed: 22885007]

56. Streich FC Jr., and Lima CD. (2016). Capturing a substrate in an activated RING E3/E2-SUMO complex. Nature 536, 304–308. 10.1038/nature19071. [PubMed: 27509863]

57. Cappadocia L, and Lima CD. (2018). Ubiquitin-like Protein Conjugation: Structures, Chemistry, and Mechanism. Chem Rev 118, 889–918. 10.1021/acs.chemrev.6b00737. [PubMed: 28234446]

58. Scott DC, Sviderskiy VO, Monda JK, Lydeard JR, Cho SE, Harper JW, and Schulman BA. (2014). Structure of a RING E3 trapped in action reveals ligation mechanism for the ubiquitin-like protein NEDD8. Cell 157, 1671–1684. 10.1016/j.cell.2014.04.037. [PubMed: 24949976]

59. Brown NG, Watson ER, Weissmann F, Jarvis MA, VanderLinden R, Grace CRR, Frye JJ, Qiao R, Dube P, Petzold G, et al. (2014). Mechanism of polyubiquitination by human anaphase-promoting complex: RING repurposing for ubiquitin chain assembly. Mol Cell 56, 246–260. 10.1016/j.molcel.2014.09.009. [PubMed: 25306923]

60. Dou H, Buetow L, Hock A, Sibbet GJ, Vousden KH, and Huang DT. (2012). Structural basis for autoinhibition and phosphorylation-dependent activation of c-Cbl. Nat Struct Mol Biol 19, 184–192. 10.1038/nsmb.2231. [PubMed: 22266821]

61. Blom N, Gammeltoft S, and Brunak S. (1999). Sequence and structure-based prediction of eukaryotic protein phosphorylation sites. J Mol Biol 294, 1351–1362. 10.1006/jmbi.1999.3310. [PubMed: 10600390]

62. Padmanabha R, Chen-Wu JL, Hanna DE, and Glover CV. (1990). Isolation, sequencing, and disruption of the yeast CKA2 gene: casein kinase II is essential for viability in Saccharomyces cerevisiae. Mol Cell Biol 10, 4089–4099. 10.1128/mcb.10.8.4089-4099.1990. [PubMed: 2196445]

63. Nguyen N, Yi JS, Park H, Lee JS, and Ko YG. (2014). Mitsugumin 53 (MG53) ligase ubiquitinates focal adhesion kinase during skeletal myogenesis. J Biol Chem 289, 3209–3216. 10.1074/jbc.M113.525154. [PubMed: 24344130]

64. Yi JS, Park JS, Ham YM, Nguyen N, Lee NR, Hong J, Kim BW, Lee H, Lee CS, Jeong BC, et al. (2013). MG53-induced IRS-1 ubiquitination negatively regulates skeletal myogenesis and insulin signalling. Nat Commun 4, 2354. 10.1038/ncomms3354. [PubMed: 23965929]
65. Rodl S, den Brave F, Raschle M, Kizmaz B, Lenhard S, Groh C, Becker H, Zimmermann J, Morgan B, Richling E, et al. (2023). The metabolite-controlled ubiquitin conjugase Ubc8 promotes mitochondrial protein import. Life Sci Alliance 6. 10.26508/lsa.202201526.
66. Oh JH, Hyun JY, Chen SJ, and Varshavsky A. (2020). Five enzymes of the Arg/N-degron pathway form a targeting complex: The concept of superchanneling. Proc Natl Acad Sci U S A 117, 10778–10788. 10.1073/pnas.2003043117. [PubMed: 32366662]
67. Borgo C, D'Amore C, Sarno S, Salvi M, and Ruzzene M. (2021). Protein kinase CK2: a potential therapeutic target for diverse human diseases. Signal Transduct Target Ther 6, 183. 10.1038/s41392-021-00567-7. [PubMed: 33994545]
68. Harper JW, and Schulman BA. (2021). Cullin-RING Ubiquitin Ligase Regulatory Circuits: A Quarter Century Beyond the F-Box Hypothesis. Annu Rev Biochem 90, 403–429. 10.1146/annurev-biochem-090120-013613. [PubMed: 33823649]
69. Xia C, Tao Y, Li M, Che T, and Qu J. (2020). Protein acetylation and deacetylation: An important regulatory modification in gene transcription (Review). Exp Ther Med 20, 2923–2940. 10.3892/etm.2020.9073. [PubMed: 32855658]
70. Marin O, Bustos VH, Cesaro L, Meggio F, Pagano MA, Antonelli M, Allende CC, Pinna LA, and Allende JE. (2003). A noncanonical sequence phosphorylated by casein kinase 1 in beta-catenin may play a role in casein kinase 1 targeting of important signaling proteins. Proc Natl Acad Sci U S A 100, 1019310200. 10.1073/pnas.1733909100.
71. Kaiser SE, Riley BE, Shaler TA, Trevino RS, Becker CH, Schulman H, and Kopito RR. (2011). Protein standard absolute quantification (PSAQ) method for the measurement of cellular ubiquitin pools. Nat Methods 8, 691–696. 10.1038/nmeth.1649. [PubMed: 21743460]
72. Chen I, Dorr BM, and Liu DR. (2011). A general strategy for the evolution of bond-forming enzymes using yeast display. Proc Natl Acad Sci U S A 108, 11399–11404. 10.1073/pnas.1101046108. [PubMed: 21697512]
73. Biyani N, Righetto RD, McLeod R, Caujolle-Bert D, Castano-Diez D, Goldie KN, and Stahlberg H. (2017). Focus: The interface between data collection and data processing in cryo-EM. J Struct Biol 198, 124–133. 10.1016/j.jsb.2017.03.007. [PubMed: 28344036]
74. Mastronarde DN. (2003). SerialEM: A Program for Automated Tilt Series Acquisition on Tecnai Microscopes Using Prediction of Specimen Position. Microscopy and Microanalysis 9, 1182–1183.
75. Zheng SQ, Palovcak E, Armache JP, Verba KA, Cheng Y, and Agard DA. (2017). MotionCor2: anisotropic correction of beam-induced motion for improved cryo-electron microscopy. Nat Methods 14, 331–332. 10.1038/nmeth.4193. [PubMed: 28250466]
76. Zhang K. (2016). Gctf: Real-time CTF determination and correction. J Struct Biol 193, 1–12. 10.1016/j.jsb.2015.11.003. [PubMed: 26592709]
77. Zivanov J, Nakane T, Forsberg BO, Kimanius D, Hagen WJ, Lindahl E, and Scheres SH. (2018). New tools for automated high-resolution cryo-EM structure determination in RELION-3. Elife 7. 10.7554/eLife.42166.
78. Scheres SH. (2012). RELION: implementation of a Bayesian approach to cryo-EM structure determination. J Struct Biol 180, 519–530. 10.1016/j.jsb.2012.09.006. [PubMed: 23000701]
79. Sanchez-Garcia R, Gomez-Blanco J, Cuervo A, Carazo JM, Sorzano COS, and Vargas J. (2021). DeepEMhancer: a deep learning solution for cryo-EM volume post-processing. Commun Biol 4, 874. 10.1038/s42003-021-02399-1. [PubMed: 34267316]
80. Pettersen EF, Goddard TD, Huang CC, Couch GS, Greenblatt DM, Meng EC, and Ferrin TE. (2004). UCSF Chimera--a visualization system for exploratory research and analysis. J Comput Chem 25, 1605–1612. 10.1002/jcc.20084. [PubMed: 15264254]
81. Pettersen EF, Goddard TD, Huang CC, Meng EC, Couch GS, Croll TI, Morris JH, and Ferrin TE. (2021). UCSF ChimeraX: Structure visualization for researchers, educators, and developers. Protein Sci 30, 70–82. 10.1002/pro.3943. [PubMed: 32881101]

82. Emsley P, and Cowtan K. (2004). Coot: model-building tools for molecular graphics. Acta Crystallogr D Biol Crystallogr 60, 2126–2132. 10.1107/S0907444904019158. [PubMed: 15572765]

83. Emsley P, Lohkamp B, Scott WG, and Cowtan K. (2010). Features and development of Coot. Acta Crystallogr D Biol Crystallogr 66, 486–501. 10.1107/S0907444910007493. [PubMed: 20383002]

84. Adams PD, Afonine PV, Bunkoczi G, Chen VB, Davis IW, Echols N, Headd JJ, Hung LW, Kapral GJ, Grosse-Kunstleve RW, et al. (2010). PHENIX: a comprehensive Python-based system for macromolecular structure solution. Acta Crystallogr D Biol Crystallogr 66, 213–221. 10.1107/S0907444909052925. [PubMed: 20124702]

85. Jumper J, Evans R, Pritzel A, Green T, Figurnov M, Ronneberger O, Tunyasuvunakool K, Bates R, Zidek A, Potapenko A, et al. (2021). Highly accurate protein structure prediction with AlphaFold. Nature 596, 583–589. 10.1038/s41586-021-03819-2. [PubMed: 34265844]

86. Chen VB, Arendall WB 3rd, Headd JJ, Keedy DA, Immormino RM, Kapral GJ, Murray LW, Richardson JS, and Richardson DC. (2010). MolProbity: allatom structure validation for macromolecular crystallography. Acta Crystallogr D Biol Crystallogr 66, 12–21. 10.1107/S0907444909042073. [PubMed: 20057044]

87. Schindelin J, Arganda-Carreras I, Frise E, Kaynig V, Longair M, Pietzsch T, Preibisch S, Rueden C, Saalfeld S, Schmid B, et al. (2012). Fiji: an open-source platform for biological-image analysis. Nat Methods 9, 676–682. 10.1038/nmeth.2019. [PubMed: 22743772]

88. Perez-Riverol Y, Bai J, Bandla C, Garcia-Seisdedos D, Hewapathirana S, Kamatchinathan S, Kundu DJ, Prakash A, Frericks-Zipper A, Eisenacher M, et al. (2022). The PRIDE database resources in 2022: a hub for mass spectrometrybased proteomics evidences. Nucleic Acids Res 50, D543–D552. 10.1093/nar/gkab1038. [PubMed: 34723319]

89. Janke C, Magiera MM, Rathfelder N, Taxis C, Reber S, Maekawa H, Moreno-Borchart A, Doenges G, Schwob E, Schiebel E, and Knop M. (2004). A versatile toolbox for PCR-based tagging of yeast genes: new fluorescent proteins, more markers and promoter substitution cassettes. Yeast 21, 947–962. 10.1002/yea.1142. [PubMed: 15334558]

90. Knop M, Siegers K, Pereira G, Zachariae W, Winsor B, Nasmyth K, and Schiebel E. (1999). Epitope tagging of yeast genes using a PCR-based strategy: more tags and improved practical routines. Yeast 15, 963–972. 10.1002/(SICI)10970061(199907)15:10B<963::AID-YEA399>3.0.CO;2-W. [PubMed: 10407276]

91. Storici F, and Resnick MA. (2006). The delitto perfetto approach to in vivo site-directed mutagenesis and chromosome rearrangements with synthetic oligonucleotides in yeast. Methods Enzymol 409, 329–345. 10.1016/S0076-6879(05)09019-1. [PubMed: 16793410]

92. Oh JH, Chen SJ, and Varshavsky A. (2017). A reference-based protein degradation assay without global translation inhibitors. J Biol Chem 292, 21457–21465. 10.1074/jbc.M117.814236. [PubMed: 29122887]

93. Gibson DG, Young L, Chuang RY, Venter JC, Hutchison CA 3rd, and Smith HO. (2009). Enzymatic assembly of DNA molecules up to several hundred kilobases. Nat Methods 6, 343–345. 10.1038/nmeth.1318. [PubMed: 19363495]

94. Weissmann F, Petzold G, VanderLinden R, Huis In ‘t Veld PJ, Brown NG, Lampert F, Westermann S, Stark H, Schulman BA, and Peters JM. (2016). biGBac enables rapid gene assembly for the expression of large multisubunit protein complexes. Proc Natl Acad Sci U S A 113, E2564–2569. 10.1073/pnas.1604935113. [PubMed: 27114506]

95. Grankowski N, Boldyreff B, and Issinger OG. (1991). Isolation and characterization of recombinant human casein kinase II subunits alpha and beta from bacteria. Eur J Biochem 198, 25–30. 10.1111/j.1432-1033.1991.tb15982.x. [PubMed: 2040287]

96. Steger M, Demichev V, Backman M, Ohmayer U, Ihmor P, Muller S, Ralser M, and Daub H. (2021). Time-resolved in vivo ubiquitinome profiling by DIA-MS reveals USP7 targets on a proteome-wide scale. Nat Commun 12, 5399. 10.1038/s41467-021-25454-1. [PubMed: 34518535]

97. Pierce NW, Kleiger G, Shan SO, and Deshaies RJ. (2009). Detection of sequential polyubiquitylation on a millisecond timescale. Nature 462, 615–619. 10.1038/nature08595. [PubMed: 19956254]

98. Demichev V, Messner CB, Vernardis SI, Lilley KS, and Ralser M. (2020). DIA-NN: neural networks and interference correction enable deep proteome coverage in high throughput. Nat Methods 17, 41–44. 10.1038/s41592-019-0638-x. [PubMed: 31768060]

99. Schafer IB, Yamashita M, Schuller JM, Schussler S, Reichelt P, Strauss M, and Conti E. (2019). Molecular Basis for poly(A) RNP Architecture and Recognition by the Pan2-Pan3 Deadenylase. Cell 177, 1619–1631 e1621. 10.1016/j.cell.2019.04.013. [PubMed: 31104843]

100. Nayak D, and Sivaraman J. (2018). Structure of LNX1:Ubc13~Ubiquitin Complex Reveals the Role of Additional Motifs for the E3 Ligase Activity of LNX1. J Mol Biol 430, 1173–1188. 10.1016/j.jmb.2018.02.016. [PubMed: 29496391]

101. Buetow L, Gabrielsen M, Anthony NG, Dou H, Patel A, Aitkenhead H, Sibbet GJ, Smith BO, and Huang DT. (2015). Activation of a primed RING E3-E2ubiquitin complex by non-covalent ubiquitin. Mol Cell 58, 297–310. 10.1016/j.molcel.2015.02.017. [PubMed: 25801170]

102. Magnussen HM, Ahmed SF, Sibbet GJ, Hristova VA, Nomura K, Hock AK, Archibald LJ, Jamieson AG, Fushman D, Vousden KH, et al. (2020). Structural basis for DNA damage-induced phosphoregulation of MDM2 RING domain. Nat Commun 11, 2094. 10.1038/s41467-020-15783-y. [PubMed: 32350255]

103. Dou H, Buetow L, Sibbet GJ, Cameron K, and Huang DT. (2013). Essentiality of a non-RING element in priming donor ubiquitin for catalysis by a monomeric E3. Nat Struct Mol Biol 20, 982–986. 10.1038/nsmb.2621. [PubMed: 23851457]

104. Patel A, Sibbet GJ, and Huang DT. (2019). Structural insights into non-covalent ubiquitin activation of the cIAP1-UbcH5B approximately ubiquitin complex. J Biol Chem 294, 1240–1249. 10.1074/jbc.RA118.006045. [PubMed: 30523153]

Highlights

- Multisite phosphorylation of an E2 enzyme mediates E3 binding in vitro and in vivo
- Multisite phosphorylation determines dedicated Ubc8-GID and UBE2H-CTLH E2-E3 pairing
- Phosphorylated E2 C-termini engage evolutionarily correlated E3 basic patches
- Flexing oligomeric E3 channels substrate to multiple rigidly placed E2 active sites

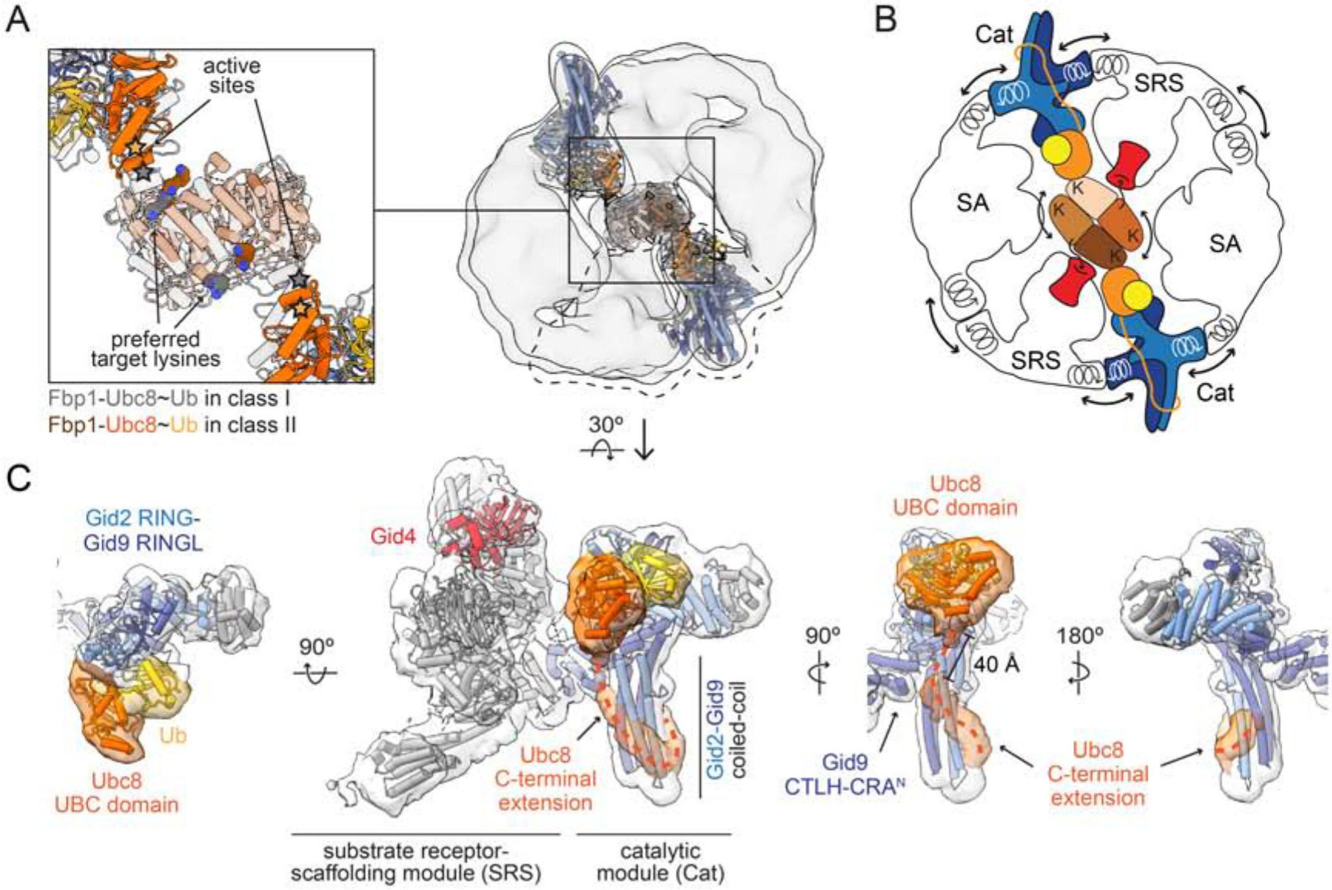

Figure 1: Dedicated GID-Ubc8 E3-E2 pair is configured for channeling a flexibly-tethered folded substrate

A. Overlay of representative cryo-EM maps (right, class I and II in Figure S2A) illustrating flexing of Chelator-GID^{SR4} and repositioning of the centrally-captured Fbp1 substrate (PDB 7NS5). Close-up (left) depicts varying positions of Ubc8~ubiquitin active sites (stars) and preferential Fbp1 target lysines (shown as spheres). Models fit into class I and II are, respectively, colored grey or color-coded (Gid2, sky blue; Gid9, navy; Ubc8, orange; ubiquitin, yellow).

B. Cartoon representing substrate channeling permitted by: (1) spring-like helical connections between substrate receptor-scaffolding (SRS), catalytic (Cat) and supramolecular assembly (SA) modules, (2) flexible tethering of folded Fbp1 domains displaying target lysines with two N-terminal degrons (black arrows) anchored to two opposing substrate receptor Gid4 molecules (red), (3) constrained configuration of the catalytic module.

C. Bipartite interactions between Ubc8~ubiquitin and Gid2-Gid9 catalytic module revealed in a 5-Å-resolution focused-refined map (around regions indicated with a black dashed line in (A)). The map was docked with models of Cat and SRS modules (Gid1-Gid5-Gid8 in grey, Gid4 in red), and Ubc8~ubiquitin. A meandering electron density around Gid2-Gid9 coiled-coil was assigned as Ubc8 C-terminal extension (orange dashed line).

See also Figures S1 and S2, Table S1, and Video S1.

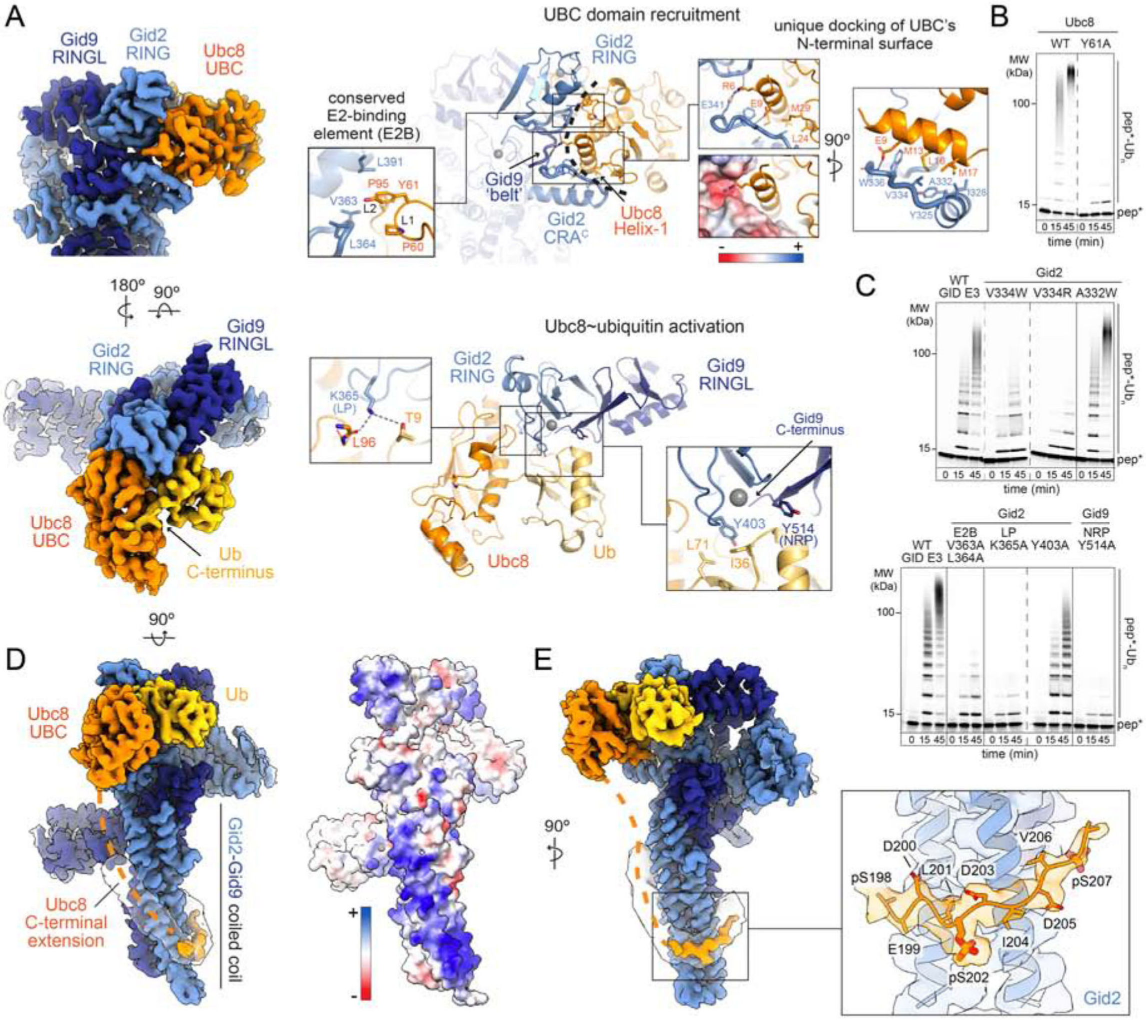

Figure 2: Molecular determinants of Ubc8~ubiquitin-Gid2-Gid9 catalytic assembly

A. Segmented 3.5-Å-resolution focused refined map of Ubc8~ubiquitin-bound Gid2-Gid9, sharpened with DeepEMhancer (left). The corresponding model (right) illustrates conserved and unique E3-E2~ubiquitin interactions mediating recruitment of ubiquitin-conjugated Ubc8's UBC domain (top) and its allosteric activation (bottom). The bowl-shaped cavity cradling the UBC domain is marked with a black dashed line.

B. Probing conserved Ubc8's UBC-Gid2 RING interactions with *in vitro* ubiquitylation assay of a fluorescently labeled model peptide substrate (pep*, harboring N-terminal Mdh2-degron connected to a single target lysine placed at position 27 via a flexible linker).

C. *In vitro* ubiquitylation assay as in (B) but with Gid2 and Gid9 mutants of residues recruiting and activating the Ubc8~ubiquitin conjugate (LP – 'linchpin' residue, E2B – canonical E2-binding interface, NRP – non-RING priming element).

D. Focused refined map as in (A) overlayed with low-resolution electron density of Ubc8 C-terminal extension (transparent) extracted from the map shown in Figure 1C. The trajectory of Ubc8 C-terminus (indicated with an orange dashed line) complements the positively-charged patch within the GID E3 catalytic module (electrostatic potential surface, right).

E. Close-up of high-resolution electron density corresponding to a distal portion of Ubc8 C-terminal extension (orange, transparent) that enabled building coordinates for its 11 residues, including sidechains of the C-terminal-most phosphoserines (pSer) 202 and 207 (orange sticks). See also Figures S1 and S2, Table S1.

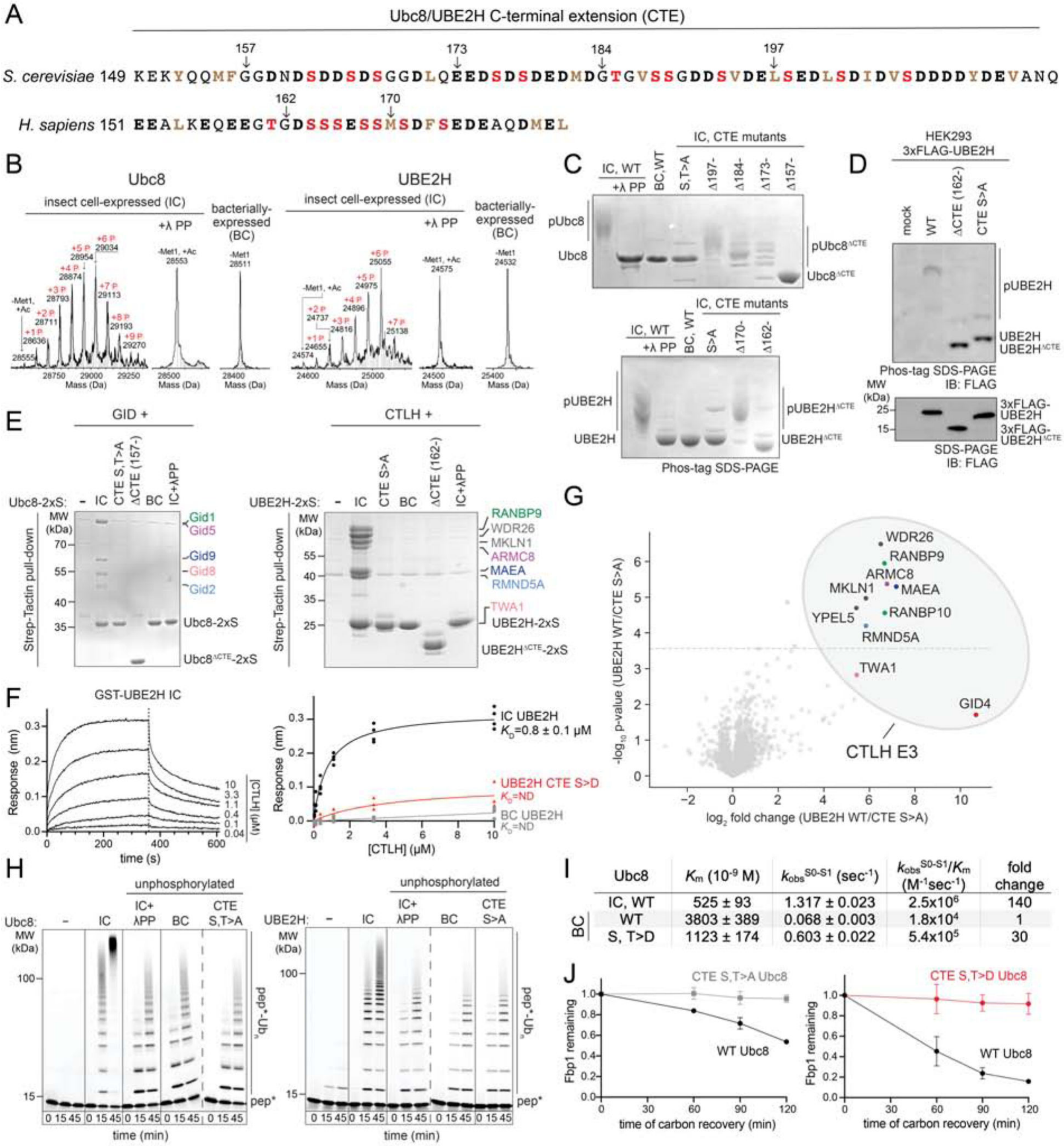

Ubc8	K_m (10^{-9} M)	k_{obs}^{S0-S1} (sec^{-1})	k_{obs}^{S0-S1}/K_m (M^{-1}sec^{-1})	fold change
IC, WT	525 ± 93	1.317 ± 0.023	2.5×10^6	140
BC WT	3803 ± 389	0.068 ± 0.003	1.8×10^4	1
BC S, T>D	1123 ± 174	0.603 ± 0.022	5.4×10^5	30

Figure 3: Multisite phosphorylated Ubc8/UBE2H C-terminal extension mediates functional partnership with GID/CTLH E3

A. C-terminal extensions of yeast Ubc8 and human UBE2H possess numerous acidic residues (bold black) and putative phosphorylation sites (bold red), flanked by irregularly distributed hydrophobics (bold brown).

B. Intact mass spectrometry analyses revealing multisite phosphorylation of insect cell-expressed (IC) C-terminally Twin-Strep-tagged yeast Ubc8 (left) and human UBE2H (right) as compared to their unphosphorylated lambda phosphatase-treated (λPP) and bacterially expressed (BC) versions. 40-Da-difference between the BC and λPP-treated IC E2s stems from N-terminal acetylation of the latter.

C. Coomassie-stained Phos-tag SDS-PAGE gels examining phosphorylation status of point mutants and truncations (indicated in (A)) of IC Ubc8 (top) and UBE2H (bottom) C-terminal extensions (CTE).

D. Assessing phosphorylation of ectopically-expressed WT and mutant 3xFLAG-UBE2H in HEK293 cells. UBE2H in Phos-tag and corresponding SDS-PAGE gels was detected by anti-FLAG immunoblotting.

E. Qualitative binding test examining capacity of different versions of C-terminally Twin-Strep-tagged Ubc8 (Ubc8–2xS) or UBE2H (UBE2H-2xS) to co-purify their recombinant untagged cognate E3s from insect cell lysates. Strep-Tactin pull-down fractions were examined with Coomassie-stained SDS-PAGE.

F. Determining binding affinity (equilibrium dissociation constant, K_D) of UBE2H for the CTLH E3 with Octet BioLayer Interferometry (BLI). The steady-state responses upon E3 binding to GST-UBE2H (right) were determined based on reference-subtracted BLI sensorgrams shown left and in Figure S4A. The unphosphorylated BC and phosphomimetic S>D UBE2H variants bound too weakly to accurately estimate K_Ds. SD (n≥3).

G. Quantitative mass-spectrometry analysis of proteins immunoprecipitated with ectopically-expressed WT and CTE S>A mutant 3xFLAG-UBE2H from HEK293 cells. Volcano plot visualizes the -log10 p-value and log2 fold change between UBE2H variants. Dotted line represents 5% q-value significance cutoff. Q-value was calculated using the Benjamini-Hochberg method for multiple testing correction. CTLH subunits are outlined with a grey oval and color-coded as in (E).

H. *In vitro* assays probing the roles of phosphorylated Ubc8/UBE2H C-terminal extension for ubiquitylation of the fluorescent model peptide substrates (pep*) designed as described in Figure 2B and harboring either Mdh2 degron or human GID4 recognition sequence PGLWRS at their N-termini for reactions mediated by $\mathrm{GID}^{\mathrm{SR4}}$ (left) and $\mathrm{CTLH}^{\mathrm{SR4}}$ (right), respectively.

I. Kinetic parameters of substrate ubiquitylation mediated by $\mathrm{GID}^{\mathrm{SR4}}$ and phosphorylated (IC), unphosphorylated (BC) or phosphomimetic (BC, S,T>D) Ubc8, estimated based on plots shown in Figure S4. The corresponding fold changes between catalytic efficiencies (k_{obs}/K_m) are calculated relative to BC Ubc8. SD, n=3.

J. *In vivo* glucose-induced degradation of exogenously expressed Fbp1–3xFLAG (quantified as a fraction of substrate remaining at different time points after switch from glucose-deplete to glucose-rich medium, normalized to the level of DHFR) in WT and Ubc8 mutant yeast strains. Error bars represent SD (n=3), points indicate the mean.

See also Figures S3 and S4.

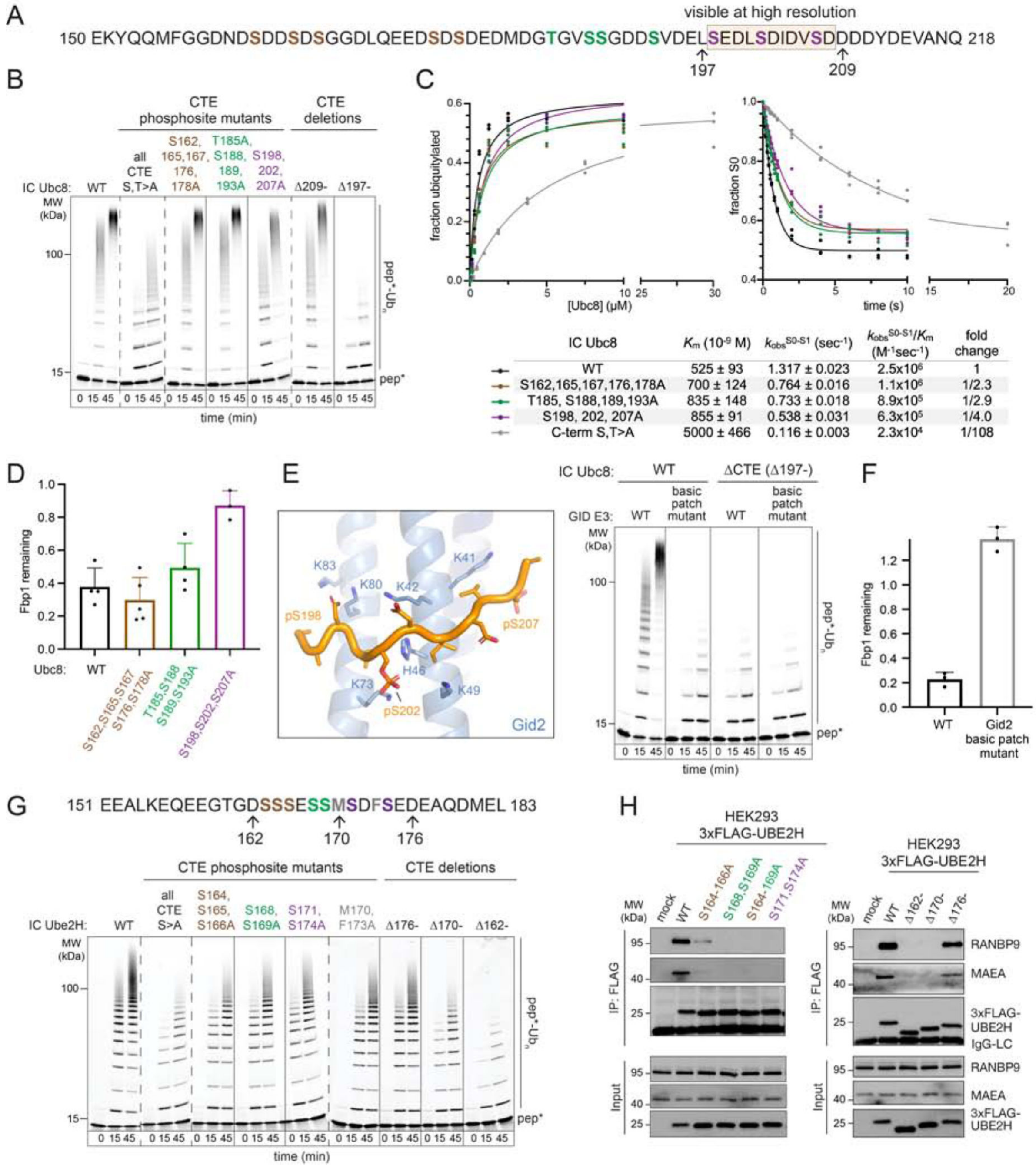

	IC Ubc8	K_m (10^{-9} M)	k_{obs}^{S0-S1} (sec^{-1})	k_{obs}^{S0-S1}/K_m (M^{-1}sec^{-1})	fold change
—●—	WT	525 ± 93	1.317 ± 0.023	2.5×10^6	1
—●—	S162,165,167,176,178A	700 ± 124	0.764 ± 0.016	1.1×10^6	1/2.3
—●—	T185, S188,189,193A	835 ± 148	0.733 ± 0.018	8.9×10^5	1/2.9
—●—	S198, 202, 207A	855 ± 91	0.538 ± 0.031	6.3×10^5	1/4.0
—●—	C-term S,T>A	5000 ± 466	0.116 ± 0.003	2.3×10^4	1/108

Figure 4: Multiple phosphorylation sites potentiate Ubc8 and UBE2H activity

A. Sequence of Ubc8 C-terminal extension indicating three subsets of phosphosites (colored brown, green and magenta) and positions of truncations used for mutational analysis. The structurally-resolved portion of the C-terminal extension is marked with an orange box.

B. Qualitative ubiquitylation assays of fluorescent model peptide (pep*) (as in Figure 2B) examining importance of individual phosphosite subsets within IC Ubc8 C-terminal extension (color-coded as in (A)) and effects of its truncations.

C. Quantitative kinetic analysis of IC Ubc8 phosphosite clusters mutants. Fitting to the plots showing the fraction of ubiquitylated Mdh2 as a function of Ubc8 concentration (left) or the time-course of Mdh2 ubiquitylation (right) represented as the fraction of remaining unmodified substrate (S_0) yielded values of K_m and k_{obs}, respectively (bottom table, SD, n=3). The fold change of catalytic efficiencies (k_{obs}/K_m) was calculated relative to WT IC Ubc8. Full kinetic plots and representative scans of SDS-PAGE gels are shown in Figure S4.

D. Effects of mutating subsets of Ubc8 phosphosites on *in vivo* degradation of yeast Fbp1–3xFLAG after 120 min of glucose recovery (relative to timepoint 0), quantified using the promoter reference technique. Error bars represent SD (n≥3).

E. Close-up of Ubc8~ubiquitin-Gid2-Gid9 model highlighting the constellation of Gid2 basic patch residues (shown as sticks) interacting with the structurally visualized portion of Ubc8 C-terminal extension (left). Mutating these Gid2 residues impeded ubiquitylation of fluorescent model peptide substrate (pep*) in reactions with WT but not C-terminally truncated (Δ197–218) IC Ubc8 (right).

F. Impact of mutating Gid2 basic patch (shown in (E)) on *in vivo* degradation of Fbp13xFLAG after 120 minutes of glucose recovery, assayed with the promoter reference technique. Error bars represent SD, n=3.

G. *In vitro* assays (bottom) testing effects of mutating individual UBE2H phosphoserine subsets and progressive truncations of its C-terminal extension (indicated in the amino acid sequence, top) on CTLH-mediated ubiquitylation of fluorescently labeled model peptide (pep*, as in Figure 3G).

H. Assessing binding of WT ectopically expressed 3xFLAG-UBE2H and its C-terminal extension mutants to endogenous CTLH. Immunoblots detect the core (RANBP9) and catalytic (MAEA) CTLH subunits as well as various 3xFLAG-UBE2H versions in the input HEK293 lysate and samples after FLAG IP.

See also Figure S4.

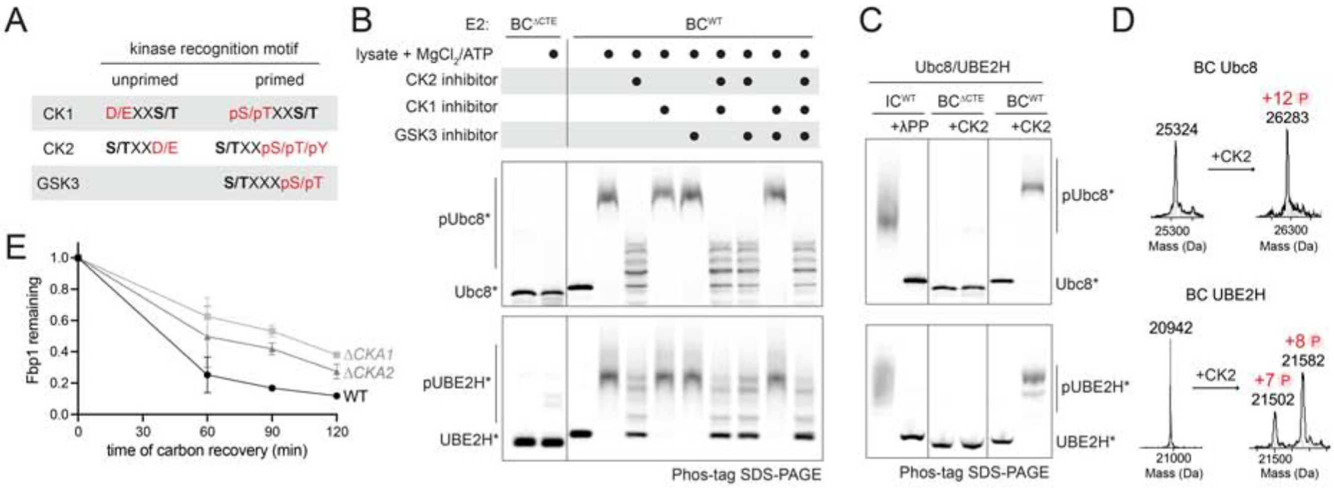

Figure 5: CK2 phosphorylates C-terminal extensions of Ubc8 and UBE2H

A. Acidophilic kinase (CK1, CK2 and GSK3) recognition motifs (red) and phosphorylation sites (black)[70].

B. Phos-tag SDS-PAGE gels assessing phosphorylation status of fluorescently labeled (*) BC Ubc8 (top) and UBE2H (bottom) after their incubation with ATP/$MgCl_2$-supplemented yeast and HEK293 lysates, respectively, with or without inhibitors of CK1, CK2 and GSK3. C-terminally truncated versions of BC Ubc8 (Δ157–218, ΔCTE) and UBE2H (Δ162–182, ΔCTE) lacking phosphorylation sites were included as negative controls.

C. A Phos-tag mobility shift assay as in (B) but examining capacity of recombinant CK2 to phosphorylate the C-terminal extensions of BC Ubc8* (top) and UBE2H* (bottom) *in vitro*.

D. Intact mass spectrometry examining phosphorylation status of CK2-treated BC Ubc86xHis and UBE2H. Numbers of conjugated phosphate groups are shown in red.

E. *In vivo* assay testing the effect of individual deletions of two CK2α isoforms (encoded by *CKA1* and *CKA2* genes) on glucose-induced degradation of exogenous Fbp1–3xFLAG in yeast, assayed with the promoter-reference technique. Error bars represent SD (n=3), points indicate the mean.

See also Figures S4 and S5.

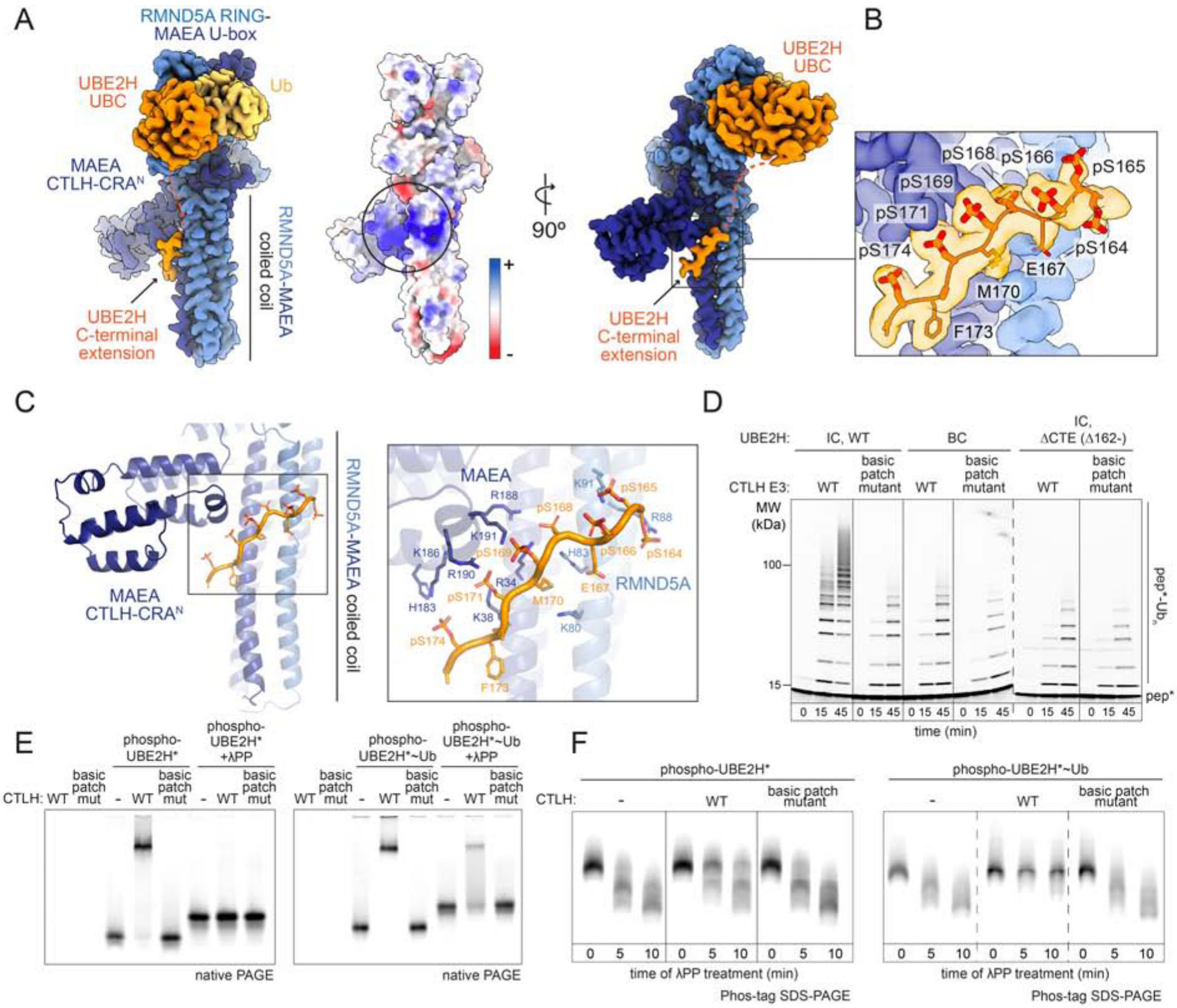

Figure 6: Multisite phosphorylated C-terminal extension of UBE2H stably engages the CTLH E3 basic patch

A. Segmented 3.4-Å-resolution focused-refined map of the UBE2H~ubiquitin-bound CTLH catalytic subunits (RMND5A, sky blue; MAEA, navy) sharpened with DeepEMhancer (left). UBE2H C-terminal extension docks into a unique RMND5A-MAEA composite basic patch (black circle) visible in the electrostatic potential surface of the catalytic module (right).

B. Close-up of electron density corresponding to the CTLH-bound C-terminal extension of UBE2H (orange, transparent), highlighting coordinates for its all phosphoserines punctuated with acidic and hydrophobic residues (orange sticks).

C. Details of interactions between multiphosphorylated UBE2H C-terminal extension and CTLH basic patch (left). RMND5A and MAEA basic residues mutated in (D), (E) and (F) are shown as sticks (right).

D. *In vitro* ubiquitylation assays probing impact of mutating RMND5A-MAEA basic patch residues on ubiquitylation of a fluorescent model peptide substrate (pep*, described in

Figure 3G) in reactions with WT IC or BC, and C-terminally deleted (ΔCTE, Δ162–183) IC UBE2H.

E. Fluorescent scans of native PAGE gels examining binding of fluorescently labeled (*) UBE2H* and UBE2H*~ubiquitin to CTLH in their fully phosphorylated (phosphor-UBE2H*) and dephosphorylated (pre-treated with λPP) states to WT and basic patch mutant CTLH.

F. Assessing susceptibility of phospho-UBE2H* and phospho-UBE2H*~ubiquitin to λPP-mediated dephosphorylation in the presence and absence of CTLH E3. Dephosphorylation reactions were quenched at indicated time points and resolved by Phos-tag SDS-PAGE gels. See also Figures S6 and S7, Table S1.

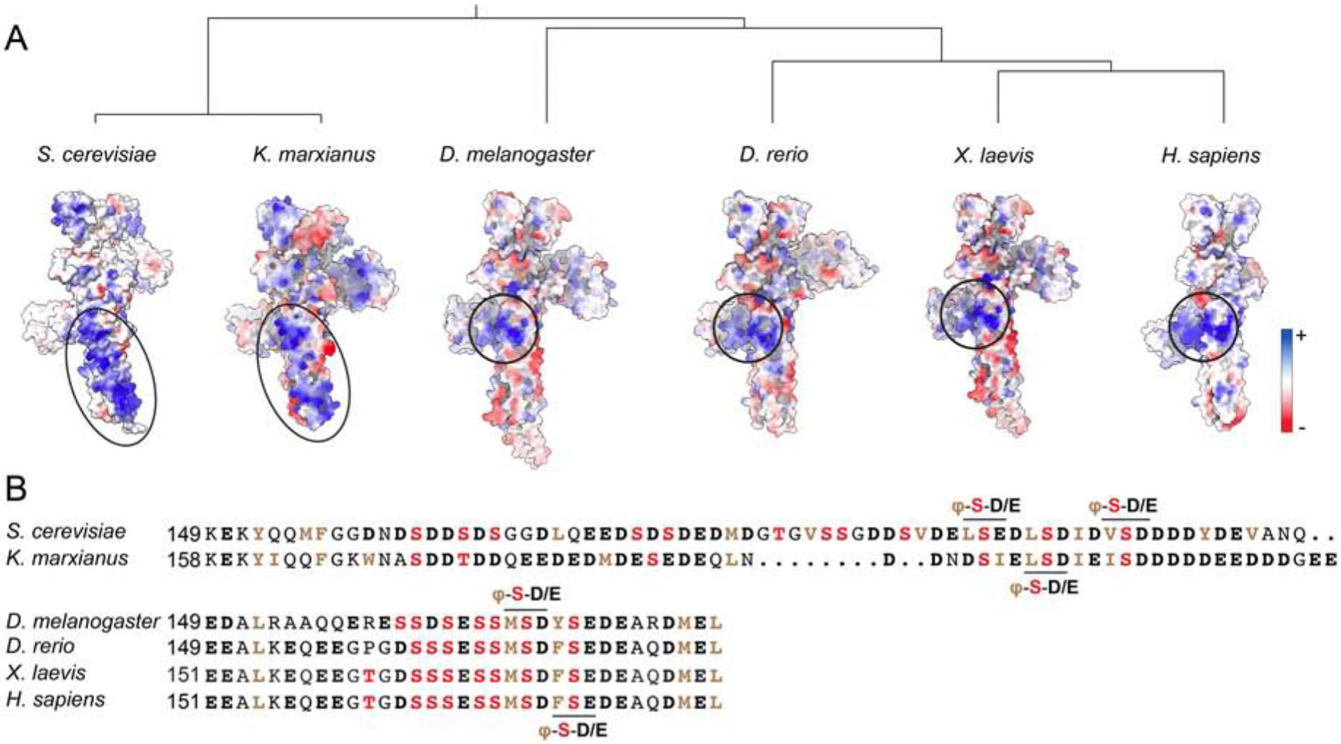

Figure 7: Evolutionary conservation of phosphorylation-mediated GID/CTLH-Ubc8/UBE2H E3-E2 pairing

A. Catalytic modules of GID/CTLH E3 orthologs represented as their electrostatic potential surfaces and displayed as a phylogenetic tree. The models were generated with AlphaFold2 (for *K. marxianus*, *D. melanogaster*, *D. rerio* and *X. laevis*) or experimentally determined (for *S. cerevisiae* and *H. sapiens*, respectively). Black ovals indicate positions of basic patches.

B. Alignment of Ubc8/UBE2H C-terminal extension sequences. Putative phosphorylation sites (red), acidic (black) and hydrophobic (brown) residues are bold and colored. Patterns of residues flanking the distal phosphosites are indicated above sequences (ϕ denotes hydrophobic residue).

KEY RESOURCES TABLE

REAGENT or RESOURCE	**SOURCE**	**IDENTIFIER**
Antibodies		
Mouse monoclonal anti-FLAG M2	Sigma	Cat#F1804; RRID: AB_262044
Rabbit anti-HA	Sigma	Cat#H6908; RRID: AB_260070
Goat anti-rabbit IgG DyLight 488-conjugated	Invitrogen	Cat#35552; RRID: AB_844398
Goat anti-mouse IgG DyLight 633-conjugated	Invitrogen	Cat#35512; RRID: AB_1307538
Goat anti-rabbit IgG peroxidase-conjugated	Sigma	Cat#A9169; RRID: AB_258434
Goat anti-mouse IgG peroxidase-conjugated	Sigma	Cat#A4416; RRID: AB_258167
Sheep polyclonal anti-MAEA	R&D Systems	Cat#AF7288-SP, RRID: AB_10971438
Rabbit polyclonal anti-RANBP9	Abnova	Cat#PAB16671; RRID: AB_10677213
Sheep polyclonal anti-UBE2H	[27]	N/A
Bacterial and Virus Strains		
E. coli BL21 RIL (DE3)	MPIB	N/A
E. coli DH5α	MPIB	N/A
Chemicals, Peptides, and Recombinant Proteins		
complete EDTA free protease inhibitor cocktail	Roche	Cat#05056489001
Aprotinin from bovine lung	Sigma	Cat#A1153-10MG
Leupeptin	Sigma	Cat#L2884-250MG
Sodium Fluoride	Sigma	Cat#201154-100G
β-glycerophosphate	Sigma	Cat#G9422-100G
Orthovanadate	NEB	Cat#P0758S
CK2	NEB	Cat#P6010L
Lambda phosphatase	NEB	Cat#P0753L
Silmitasertib (CX-4945)	Selleckchem	Cat#S0707
SML0795	Sigma	Cat#SML0795-5MG
PZ0313	Sigma	Cat#PZ0313-5MG
Phos-tag Acrylamide	FUJIFILM Wako Chemicals	Cat#304-93521
BODIPY maleimide	ThermoFisher Scientific	Cat#B10250
Peptide: GGGGGFYVK-FAM	MPIB	N/A
Peptide: PHSVTPSIEQDSLK	MPIB	N/A
Peptide: PHSVTPSIEDSTEGFTGRGWSGRGWSKGGK-FAM	MPIB	N/A
Peptide: PGLWRSPRRDSTEGFTGRGWSGRGWSKGGK-FAM	MPIB	N/A
Critical Commercial Assays		
Octet anti-GST Biosensors	Sartorius	Cat#18-5096

REAGENT or RESOURCE	**SOURCE**	**IDENTIFIER**
Deposited Data		
Chelator-GID^{SR4}-Fbp1-phospho-Ubc8~ubiquitin: class I	This paper	EMD-17705
Chelator-GID^{SR4}-Fbp1-phospho-Ubc8~ubiquitin: class II	This paper	EMD-17706
Chelator-GID^{SR4}-Fbp1-phospho-Ubc8~ubiquitin: class III	This paper	EMD-17707
Chelator-GID^{SR4}-Fbp1-phospho-Ubc8~ubiquitin: class IV	This paper	EMD-17710
Chelator-GID^{SR4}-Fbp1-phospho-Ubc8~ubiquitin: class V	This paper	EMD-17709
SRS and Cat modules of yeast Chelator-GID^{SR4} bound to multiphosphorylated Ubc8~ubiquitin	This paper	EMD-17717
Catalytic module of yeast GID E3 ligase bound to multiphosphorylated Ubc8~ubiquitin	This paper	EMD-17764; PDB: 8PMQ
CTLH^{SR4}-phospho-UBE2H~ubiquitin bound to engineered VH	This paper	EMD-17716
SRS and Cat modules of human CTLH^{SR4} bound to multiphosphorylated UBE2H~ubiquitin	This paper	EMD-17715
Catalytic module of human CTLH E3 ligase bound to multiphosphorylated UBE2H~ubiquitin	This paper	EMD-17713; PDB: 8PJN
Raw image data	This paper	Mendeley Data: http://dx.doi.org/10.17632/cydfk4y8ty.1
Proteomics data	This paper	Table S2; PRIDE: PXD043646
Experimental Models: Cell Lines		
T. ni: High Five	ThermoFisher Scientific	Cat#B85502
Human: Flp-In-T-REx-HEK293	ATCC	Cat#CRL-1573; RRID: CVCL_U427
Human: Flp-In-T-REx-HEK293 + 3xFLAG-MAEA	This paper	N/A
Human: Flp-In-T-REx-HEK293 + 3xFLAG-MAEA R34A, K38A, R188A, K191A, K186A, H183A, R190A (basic patch mutant)	This paper	N/A
Experimental Models: Organisms/Strains		
S. cerevisiae: Strain S288C: BY4741; MATa his3Δ1 leu2Δ0 met15Δ0 ura3Δ0	Euroscarf	Cat#Y00000
S. cerevisiae: BY4741; Cka2::KANMX4	This paper	N/A
S. cerevisiae: BY4741; Cka1::KANMX4	This paper	N/A
S. cerevisiae: BY4741; Gid2::3xFLAG-Gid2	This paper	N/A
S. cerevisiae: BY4741; Gid2::3xFLAG-Gid2 K41A, K42A, H46A, K49A, K73A, K80A, K83A (basic patch mutant)	This paper	N/A
S. cerevisiae: BY4741; Ubc8::Ubc8-Myc S162A, S165A, S167A, S176A, S178A, T185A, S188A, S189A, S193A, S198A, S202A, S207A (CTE S,T>A)	This paper	N/A
S. cerevisiae: BY4741; Ubc8::Ubc8-Myc, Gid7::NATNT2	This paper	N/A
S. cerevisiae: BY4741; Ubc8::Ubc8-Myc CTE S,T>A, Gid7::NATNT2	This paper	N/A
S. cerevisiae: BY4741; Ubc8::Ubc8-Myc S162D, S165D, S167D, S176D, S178D, T185D, S188D, S189D, S193D, S198D, S202D, S207D (CTE S,T>D)	This paper	N/A
S. cerevisiae: BY4741; Ubc8::Ubc8-Myc	This paper	N/A
S. cerevisiae: BY4741; Ubc8::Ubc8 (S162,165,167,176,178A)-V5-8xHis	This paper	
S. cerevisiae: BY4741; Ubc8::Ubc8(T185.S189,193A)-V5-8xHis	This paper	N/A

REAGENT or RESOURCE	SOURCE	IDENTIFIER
S. cerevisiae: BY4741; Ubc8::Ubc8(S198,202,207A)-V5-8xHis	This paper	N/A
S. cerevisiae: BY4741::Ubc8::Ubc8 (first5bp+intron)-pCORE-V5-8xHis	This paper	N/A
Recombinant DNA		
pCSJ95	[40]	N/A
pCSJ125	[40]	N/A
pBIG2 Gid1:Gid8-TEV-2xS:Gid5:Gid4:Gid2:Gid9	[36]	N/A
pBIG2 Gid1:Gid8-TEV-2xS:Gid5:Gid4:Gid2:Gid9:Gid7	[37]	N/A
pBIG2 Gid1:Gid8-TEV-2xS:Gid5:Gid4:Gid9	[36]	N/A
pBIG2 Gid1:Gid8-TEV-2xS:Gid5:Gid4:Gid2	[36]	N/A
pBIG2 Gid1:Gid8:Gid5: Gid2:Gid9	This paper	N/A
pBIG1a Gid1:Gid8-TEV-2xS:Gid5:Gid4	This paper	N/A
pBIG2 RANBP9:TWA1-TEV-2xS:ARMC8:RMND5A:MAEA	[37]	N/A
pBIG2 RANBP9:TWA1-TEV-2xS:ARMC8:RMND5A	[37]	N/A
pBIG2 RANBP9:TWA1-TEV-2xS:ARMC8:MAEA	[37]	N/A
pBIG1a RANBP9:TWA1-TEV-2xS:ARMC8	This paper	N/A
pBIG2 RANBP9:TWA1-TEV-2xS:RMND5A:MAEA	This paper	N/A
pBIG2 RANBP9:TWA1: ARMC8:RMND5A:MAEA: WDR26:MKLN1	This paper	N/A
pLIB Ubc8-TEV-2xS	This paper	N/A
pLIB Ubc8-TEV-2xS (Δ157-218)	This paper	N/A
pLIB Ubc8-TEV-2xS (Δ173-218)	This paper	N/A
pLIB Ubc8-TEV-2xS (Δ184-218)	This paper	N/A
pLIB Ubc8-TEV-2xS (Δ197-218)	This paper	N/A
pLIB Ubc8-TEV-2xS (Δ209-218)	This paper	N/A
pLIB Ubc8-TEV-2xS S162A, S165A, S167A, S176A, S178A, T185A, S188A, S189A, S193A, S198A, S202A, S207A (CTE S,T>A)	This paper	N/A
pLIB Ubc8-TEV-2xS S162A, S165A, S167A, S176A, S178A	This paper	N/A
pLIB Ubc8-TEV-2xS T185A, S188A, S189A, S193A	This paper	N/A
pLIB Ubc8-TEV-2xS S198A, S202A, S207A	This paper	N/A
pLIB Ubc8-TEV-2xS Y61A	This paper	N/A
pLIB UBE2H-TEV-2xS	This paper	N/A
pLIB UBE2H-TEV-2xS (Δ162-183)	This paper	N/A
pLIB UBE2H-TEV-2xS (Δ170-183)	This paper	N/A
pLIB UBE2H-TEV-2xS (Δ176-183)	This paper	N/A
pLIB UBE2H-TEV-2xS S164A, S165A, S166A, S168A, S169A, S171A, S174A (CTE S>A)	This paper	N/A
pLIB UBE2H-TEV-2xS S164A, S165A, S166A	This paper	N/A
pLIB UBE2H-TEV-2xS S168A, S169A	This paper	N/A
pLIB UBE2H-TEV-2xS S171A, S174A	This paper	N/A
pLIB UBE2H-TEV-2xS M170A, F173A	This paper	N/A
pLIB UBE2H-TEV-2xS F63A	This paper	N/A

REAGENT or RESOURCE	SOURCE	IDENTIFIER
pLIB Gid2 V363A, L364A	This paper	N/A
pLIB Gid2 K365A	This paper	N/A
pLIB Gid2 Y403A	This paper	N/A
pLIB Gid2 K41A, K42A, H46A, K49A, K73A, K80A, K83A (basic patch mutant)	This paper	N/A
pLIB Gid2 V334W	This paper	N/A
pLIB Gid2 V334R	This paper	N/A
pLIB Gid2 A332W	This paper	N/A
pLIB Gid9 Y514A	This paper	N/A
pLIB RMND5A I338A, L339A	This paper	N/A
pLIB RMND5A R340A	This paper	N/A
pLIB RMND5A K80A, H83A, K91A, R88A (basic patch mutant)	This paper	N/A
pLIB RMND5A C308W	This paper	N/A
pLIB RMND5A C308R	This paper	N/A
pLIB RMND5A V311W	This paper	N/A
pLIB RMND5A V311R	This paper	N/A
pLIB RMND5A R306W	This paper	N/A
pLIB MAEA Y394A	This paper	N/A
pLIB MAEA R34A, K38A, R188A, K191A, K186A, H183A, R190A (basic patch mutant)	This paper	N/A
pLIB GST-TEV-Ubc8	This paper	N/A
pLIB GST-TEV-Ubc8 S162A, S165A, S167A, S176A, S178A, T185A, S188A, S189A, S193A, S198A, S202A, S207A (CTE S,T>A)	This paper	N/A
pLIB GST-TEV-Ubc8 S162A, S165A, S167A, S176A, S178A	This paper	N/A
pLIB GST-TEV-Ubc8 T185A, S188A, S189A, S193A	This paper	N/A
pLIB GST-TEV-Ubc8 S198A, S202A, S207A	This paper	N/A
pLIB GST-TEV-Ubc8 C85K	This paper	N/A
pLIB GST-TEV-Ubc8 C85K, K133C	This paper	N/A
pLIB GST-TEV-UBE2H	This paper	N/A
pLIB GST-TEV-UBE2H C87K	This paper	N/A
pLIB GST-TEV-UBE2H C87K, E135C	This paper	N/A
pLIB 6xHis-VH-GS-UBE2H (Δ1-150)	This paper	N/A
pLIB GST-TEV-UBA1	This paper	N/A
pGEX GST-TEV-Ubc8	[36]	N/A
pGEX GST-TEV-Ubc8 S162D, S165D, S167D, S176D, S178D, T185D, S188D, S189D, S193D, S198D, S202D, S207D (CTE S,T>D)	This paper	N/A
pGEX GST-TEV-Ubc8 C85K, K133C	This paper	N/A
pGEX GST-TEV-Ubc8 (Δ157-218) C85K, K133C	This paper	N/A
pGEX GST-TEV-UBE2H	[37]	N/A
pGEX GST-TEV-UBE2H S164D, S165D, S166D, S168D, S169D, S171D, S174D (CTE S,T>D)	This paper	N/A

REAGENT or RESOURCE	SOURCE	IDENTIFIER
pGEX GST-TEV-UBE2H C87K, E135C	This paper	N/A
pGEX GST-TEV-UBE2H (Δ162-183) C87K, E135C	This paper	N/A
pGEX GST-TEV-GID4 (Δ1-99)	[37]	N/A
pGEX GST-3C-ubiquitin all K>R (K0)	[37]	N/A
pRSF Fbp1-GGGGS-sortag-6xHis	[37]	N/A
pRSF Mdh2-GGGGS-sortag-6xHis	[36]	N/A
pRSF Fbp1-6xHis	[37]	N/A
pRSF Mdh2 (K254R, K256R, K259R, K360R, K361R)-GGGGS-sortag-6xHis	[44]	N/A
pRSF Mdh2 (K254R, K256R, K259R, K330R, K360R, K361R)-6xHis	[36]	N/A
pRSF CK2a-6xHis	This paper	N/A
pQlink Ubc8-TEV-2xS	This paper	N/A
pQlink UBE2H-TEV-2xS	This paper	N/A
pET3b 6xHis-3C-ubiquitin	This paper	N/A
pET3b ubiquitin	[71]	N/A
pET29 sortase	[72]	N/A
pcDNA5a-3xFLAG-UBE2H	This paper	N/A
pcDNA5a-3xFLAG-UBE2H (Δ162-183)	This paper	N/A
pcDNA5a-3xFLAG-UBE2H (Δ170-183)	This paper	N/A
pcDNA5a-3xFLAG-UBE2H (Δ176-183)	This paper	N/A
pcDNA5a-3xFLAG-UBE2H S164A, S165A, S166A	This paper	N/A
pcDNA5a-3xFLAG-UBE2H S168A, S169A	This paper	N/A
pcDNA5a-3xFLAG-UBE2H S164A, S165A, S166A, S168A, S169A	This paper	N/A
pcDNA5a-3xFLAG-UBE2H S171A, S174A	This paper	N/A
pcDNA5a-3xFLAG-UBE2H S164A, S165A, S166A, S168A, S169A, S171A, S174A (CTE S>A)	This paper	N/A
Software and Algorithms		
Focus	[73]	https://focus.c-cina.unibas.ch/documentation.php
SerialEM v3.8.0-b5	[74]	http://bio3d.colorado.edu/SerialEM/
EPU v2.7.0	ThermoFisher Scientific	https://www.thermofisher.cn/cn/zh/home/electron-microscopy/products/software-em-3d-vis/epu-software.html
MotionCor2 v1.1	[75]	https://emcore.ucsf.edu/ucsf-software
Gctf v1.06	[76]	https://www.mrc-lmb.cam.ac.uk/kzhang/Gctf/
Gautomatch v0.56	Kai Zhang (MRC, Laboratory of Molecular Biology, Cambridge, UK)	https://www.mrc-lmb.cam.ac.uk/kzhang/Gautomatch/
Relion v4.0	[77,78]	https://github.com/3dem/relion

REAGENT or RESOURCE	SOURCE	IDENTIFIER
DeepEMhancer	[79]	https://github.com/rsanchezgarc/deepEMhancer
UCSF Chimera v1.13.1	[80]	https://www.cgl.ucsf.edu/chimera/
UCSF ChimeraX v1.5	[81]	https://www.cgl.ucsf.edu/chimerax/
PyMOL v2.5.2	Schrödinger	https://pymol.org/2/
Coot v0.9.8.7	[82,83]	https://www2.mrc-lmb.cam.ac.uk/personal/pemsley/coot/
PHENIX v1.19.2	[84]	https://www.phenix-online.org/
AlphaFold2	[85]	https://alphafold.ebi.ac.uk
Molprobity	[86]	http://molprobity.biochem.duke.edu/
ImageStudioLite software	LI-COR	https://www.licor.com/bio/image-studio/
ImageQuant TL analysis software	Cytiva	https://www.cytivalifesciences.com/
Fiji v2.0.0-rc-59/1.51j	[87]	https://imagej.net/
PRISM v9.1.0	GraphPad	https://www.graphpad.com/
Other		
R1.2/1.3, Cu 200 mesh, holey carbon grids	Quantifoil	Cat#N1-C14nCu20-01